Structure-Driven Photoluminescence Enhancement in a Zn-based Metal Organic Framework

Stephanie Jensen,[1,2] Kui Tan,[3] William P. Lustig,[4] Dmitri S. Kilin,[5] Jing Li,[4] Yves J. Chabal,[3] and Timo Thonhauser[1,2,*]

[1] *Department of Physics, Wake Forest University, Winston-Salem, NC 27109, USA*
[2] *Center for Functional Materials, Wake Forest University, Winston-Salem, NC 27109, USA*
[3] *Department of Materials Science and Engineering, University of Texas at Dallas, Richardson, TX 75080, USA*
[4] *Department of Chemistry and Chemical Biology, Rutgers University, Piscataway, NJ 08854, USA*
[5] *Department of Chemistry and Biochemistry, North Dakota State University, Fargo, ND 58108, USA*

(Dated: September 6, 2019)

We investigate the much debated mechanism which leads to an enhancement of the photoluminescence upon small aromatic molecule adsorption in the Zn-based metal organic framework (MOF) material PCP-Zn. We present evidence based on *ab initio* simulations, coupled with *in situ* IR spectroscopy and photoluminescence measurements, that (i) the PCP-Zn "turn on" photoluminescence enhancement effect upon guest molecule adsorption mainly occurs as the result of an underlying guest-induced structural change and (ii) a further, but smaller, enhancement occurs along with a change in emission color due to interactions of the guest molecules with the framework, altering the MOF's electronic structure. We provide a detailed analysis of both mechanisms. The clear separation of a dominating structural effect and minor electronic effect is important for e.g. sensing applications, where they can help to design improved MOF-based sensors with increased efficiency and selectivity.

I. INTRODUCTION

Metal organic framework (MOF) materials have a plethora of applications due to their tunability during synthesis. Popular applications include gas storage and sequestration,[1–9] catalysis,[10–13] polymerization,[14,15] energy storage,[16–18] optics,[19] multiferroics,[20–22] drug delivery,[23] and luminescence.[24–32] The latter is of particular interest in sensing applications where MOFs can undergo changes in the observed photoluminescence via quenching (loss or decrease of light emission) or enhancement (gain or increase in light emission) depending on external factors such as introduction of particular guest molecules,[28,33,34] humidity,[35] pH,[36] and even temperature.[37] Much progress has been made in the area of photoluminescent sensing MOFs and the synthesis of new MOFs with such capabilities is an active area of research;[38] unfortunately, the exact mechanisms of sensing are not always fully understood.[28,32–34,39,40] Although various mechanisms have been proposed, their experimental verification proves challenging as they involve identifying the exact guest-host interaction, electron charge transfer, ionic vibrations, and/or other atomic scale processes. Experimental studies are further complicated due to the fact that each MOF likely senses using a different mechanism which might even change depending on the analyte in question. A systematic study combining various experimental and theoretical tools is thus required.

Here, we provide such a study, focusing on ligand-to-ligand charge transfer (LLCT) photoluminescent MOFs, which are typically formed of a d^{10} metal and two fluorophore organic ligands that emit the light. The two ligands are electronically insulated by the fully occupied d orbitals of the metal clusters. During the absorption process, an electron is excited from one organic linker, forming the donor, to the other organic linker, becoming the acceptor. The electron and hole then recombine on the radiative time scale, allowing

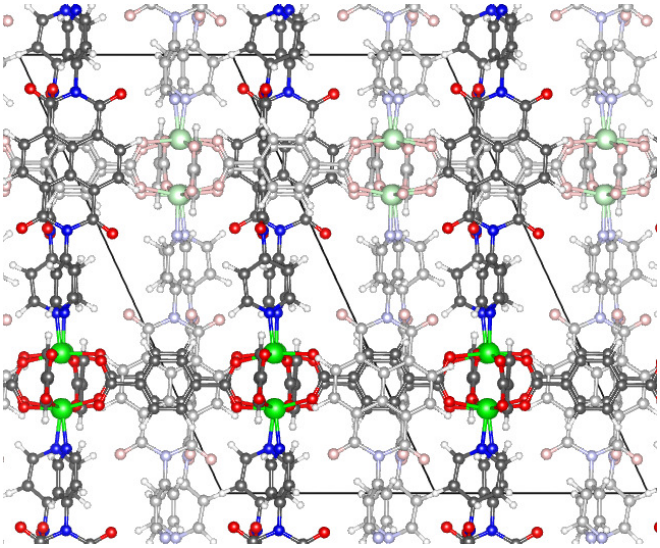

Figure 1. Unit cell of PCP-Zn, which exhibits photoluminescence enhancement upon adsorption of aromatic compounds. The empty MOF unit cell (without guest molecules) consists of two identical subframeworks, depicted here with bold and muted colors to highlight the two subframeworks. Atoms are colored as follows: C (grey), N (blue), O (red), Zn (green), and H (white).

the emission of a photon. For our study, we use the LLCT MOF PCP-Zn, a Zn-based photoluminescent MOF shown in Fig. 1, which is an entangled porous coordination polymer framework: $Zn_2(bdc)_2(dpNDI)$ [bdc = 1,4-benzenedicarboxylate; dpNDI = N,N′-di(4-pyridyl)-1,4,5,8-naphthalenediimide]. PCP-Zn exhibits significantly enhanced luminescence upon addition of aromatic analytes in general[41] and here we study the adsorption of benzene in particular. In order to investigate the corresponding mechanisms in this MOF on the atomic scale, we combine *ab initio* methods with synthesis, vibrational spectroscopy, and photoluminescence experiments. We find that the drastic change in photoluminescence is mainly due to an underlying guest-induced structural change and to a lesser extent due to guest-induced changes in the electronic structure. Our *ab initio* simulations allow us to disentangle those two effects and we analyze them both in detail below.

II. METHODS

A. Computational Details

All calculations were performed with the VASP package[42,43] at the density functional theory level (DFT), using the vdW-DF[44–47] exchange-correlation functional which captures the long-range interactions indicative of aromatic guest molecule binding in MOFs. PAW pseudopotentials were used as provided by VASP, with a 600 eV energy cutoff. Electronic relaxations were converged up to an SCF criterion of less than 1×10^{-4} eV; structural relaxations optimized the forces on all atoms to below 1 meV/Å. The empty PCP-Zn unit cell (MOF without guest molecule, see Fig. 1) contains 312 atoms, the PCP*-Zn unit cell (MOF after structural change without guest molecule) has 156 atoms, and the Bz+PCP-Zn unit cell (MOF after structural change with benzene guest molecule) contains 168 atoms. Because of the size of these unit cells, only the Γ-point was used. In order to verify IR peak assignments, vibrational frequencies were calculated from the dynamical matrix and its corresponding sum rules, using the finite differences method with a displacement of 0.01 Å.

Computational details of our methodology to assess photoluminescence properties have been thoroughly described in prior work,[48] where we have applied it successfully to explain the photoluminescence quenching in RPM3-Zn. In summary, *ab initio* Born-Oppenheimer molecular dynamics (MD) was used to capture the dynamics and evaluate the optical properties along the nuclear trajectory. To this end, a 1 ps trajectory was calculated at 27 °C with 1000 time steps of 1 fs each. The photoluminescence was then modeled by calculating the oscillator strength at each time step of the MD trajectory as

$$f_{ij}\big(\{\mathbf{R}_\mathrm{I}(t)\}\big) = \frac{4\pi m_e \omega_{ij}}{3\hbar e^2}\left|\mathbf{D}_{ij}\big(\{\mathbf{R}_\mathrm{I}(t)\}\big)\right|^2 , \qquad (1)$$

where e and m_e are the charge and mass of the electron, $\omega_{ij} = (\varepsilon_i - \varepsilon_j)/\hbar$ is the energy difference between the states i and j, $\{\mathbf{R}_\mathrm{I}(t)\}$ are the ionic positions at time t, and $\mathbf{D}_{ij}$ is the transition dipole moment

$$\mathbf{D}_{ij}\big(\{\mathbf{R}_\mathrm{I}(t)\}\big) = e\int \psi_i^*\big(\{\mathbf{R}_\mathrm{I}(t)\}\big)\ \mathbf{r}\ \psi_j\big(\{\mathbf{R}_\mathrm{I}(t)\}\big)\ d^3r\ . \qquad (2)$$

We have considered all possible transitions between the 176 unoccupied states (i) and the 592 occupied states (j), although the most interesting transitions in the visible range are within 10 states of the valence and conduction band edges and photoluminescence is known to be mostly the result of a transition from LUMO to HOMO.[49] The "scissors" operator is used as a post-processing step to adjust the calculated Kohn-Sham band gap to our experimentally measured one, with a justification provided in Ref. [48]. From the MD trajectory we can also calculate the non-adiabatic electronic couplings and, in turn, the non-radiative lifetimes of the various excited electron and hole states. Further details can be found in Ref. [48] and the SI, including verification of approximations made at the level of theory and the method for calculating thermal ellipsoids images from the MD trajectory.

B. Characterization

Fluorescence spectra were collected at room temperature under 330 nm excitation using a Horiba FluoroMax-4 spectrophotometer. Powder X-ray diffraction data were collected at room temperature on a Rigaku Ultima VI diffractometer using Cu K_α radiation (λ = 1.5406 Å). The structure and purity of the dpNDI ligand were confirmed using a Varian VNMRS 400 MHz NMR at room temperature (see Fig. S1). Diffuse reflectance spectra were collected at room temperature on a Shimadzu UV-3600 spectrophotometer with an integrating sphere attachment and converted to the Kubelka Munk function.

Our *in situ* infrared (IR) spectra were taken in the following way: A powder sample of PCP-Zn (2 mg) was pressed onto a KBr pellet and placed into a vacuum cell purchased from Specac at the focal point of the sample compartment of the infrared spectrometer (Nicolet 6700, Thermo Scientific) equipped with a liquid N_2-cooled MCT-A detector. The cell is connected to a vacuum line for evacuation (base pressure < 20 mTorr). Prior to benzene vapor exposure at room temperature, the sample was activated by annealing (150 °C) for at least 3 hours in vacuum to remove adsorbed solvents and H_2O. Vapors of benzene were then introduced into the vacuum cell at 1 Torr and spectra were recorded during the exposure and after evacuation of gas-phase benzene in transmission mode between 650 and 4000 cm^{-1} (4 cm^{-1} spectral resolution). The spectra of gas phase benzene were measured after introducing benzene vapors to the cell with a blank KBr pellet for comparison with the adsorbed Bz+PCP-Zn. A discussion on the stability

of PCP-Zn following this procedure can be found in the SI along with additional characterization (Fig. S2).

C. Synthesis

All reagents were purchased from Sigma Adlrich and used without additional purification. The ligand N,N′-di(4-pyridyl)-1,4,5,8-naphthalenetetracarboxydiimide (dpNDI) was synthesized using a reported method (for further details see the supplementary materials).[50] PCP-Zn was synthesized solvothermally;[41] 0.50 mmol of $Zn(NO_3)_6$ H_2O (0.149 g), 0.50 mmol of dpNDI (0.210 g), and 0.05 mmol of benzene-1,4-dicarboxylic acid (H_2bdc, 0.083 g) were combined in 50 mL DMF, sonicated until finely suspended, and then heated at 95 °C for three days. The resulting yellow crystals were recovered via filtration to give the as-made DMF+PCP-Zn. The crystals were then dried under vacuum at 120 °C overnight to give the outgassed PCP-Zn. To generate the solvated Bz+PCP-Zn, samples of the outgassed PCP-Zn were immersed in 20 mL of the relevant solvent for ten days. Powder X-ray diffraction was used to ensure that all samples were the correct phase (Figs. S3, S4, and S5).

III. RESULTS & DISCUSSION

The enhancement of photoluminescence by aromatic guest species in PCP-Zn was first published in Ref. [41]. The empty PCP-Zn shows so little photoluminescence that it is considered to be in an "off" state. However, upon adsorption of aromatic guest molecules, PCP-Zn undergoes a transition which in general results in (i) a large increase in photoluminescence and (ii) a guest-molecule-dependent color shift of the photoluminescence. For example, PCP-Zn without guest has a quantum yield of less than 0.01, which increases dramatically upon the introduction of aromatic guest molecules such as benzene (0.05) and toluene (0.22).[41] In the following, we analyze this "off to on" transition with a combination of experimental and theoretical tools. For our study we focus on the adsorption of benzene, which—in contrast to e.g. toluene—shows no change in color emission.[41] To this end, we consider the three systems depicted in Fig. 2: the empty PCP-Zn system, the corresponding system loaded with benzene referred to as Bz+PCP-Zn, and an artificial system called PCP*-Zn, which has the Bz+PCP-Zn structure but without the benzene guest molecule. Simulations on the latter system allow us to disentangle structural and electronic effects on the photoluminescence enhancement.

Figure 3 shows the results for our experimental and computational photoluminescence spectra, identifying two distinct mechanisms for the observed enhancement. While both effects are brought on by introducing the benzene guest molecule, the mechanisms are distinctly separate: (i) the *structure change* from PCP-Zn to PCP*-Zn without adding the benzene accounts for an impressive 394% increase in photoluminescence intensity and (ii) adding the benzene into the structure PCP*-Zn to arrive at Bz+PCP-Zn causes a smaller *electronic structure change* that accounts merely for another 58% increase. These observed measurements are comparable to the previously published results where the quantum yield increased from less than 0.01 to 0.05 upon introduction of benzene into PCP-Zn.[41] The first effect is discussed in detail in Section III A and the latter in Section III B by analyzing changes in band structure and nonradiative electron/hole relaxation rates. Other mechanisms have also been suggested to increase photoluminescence such as charge transfer to the guest molecule (guest-induced trap state)[28] or decreasing ionic vibrations.[28,33] However, in the system under study we can rule out guest-induced trap states for reasons discussed at the end of Section III B. We also find that the ionic vibrations are similar with and without the benzene guest molecule (see Fig. S6) and actually increase somewhat upon benzene adsorption. Thus, guest-induced rigidifcation of the MOF framework can also be eliminated as an enhancement mechanism.

A. Structural Induced Enhancement

The structure of PCP-Zn consists of two identical subframeworks composed of a metal node connected to four bdc and two dpNDI ligands. The metal node is made up of two Zn atoms, which are each connected to four oxygen and one nitrogen. In the PCP-Zn structure the two subframeworks are highly interconnected and not perpendicular, as seen in Figs. 2a, 2d, and 2g. The face of the dpNDI ligand of one subframework faces two bdc ligand aromatic rings of the other subframework; however, it is closer to one bdc ring than the other. Once the benzene guest molecule is introduced, the subframeworks shift with respect to each other. The unit cell is no longer triclinic but rather orthorhombic, indicating the two subframeworks are nearly perpendicular to each other, see Fig. 2c, 2f, and 2i. The dpNDI still faces two bdc ligands, but the centers align moreso than in the PCP-Zn. The benzene binds in the larger of the two spaces between a dpNDI and bdc (Fig. 2i). The more perpendicular alignment of the two subframeworks and slight shift of the dpNDI with respect to the bdc are the major differences between PCP-Zn and Bz+PCP-Zn. After the structure change, the unit cell can now be described with half as many atoms, with two metal nodes per unit cell (one for each subframework) as opposed to the four needed (two for each subframework) to describe the PCP-Zn unit cell. Both the structural rearrangement and the location of the aromatic guest molecule were determined through single crystal analysis.[41]

By using the Bz+PCP-Zn unit cell but removing the benzene, we arrive at the artificial structure PCP*-Zn, which allows us to study the effect of the structural

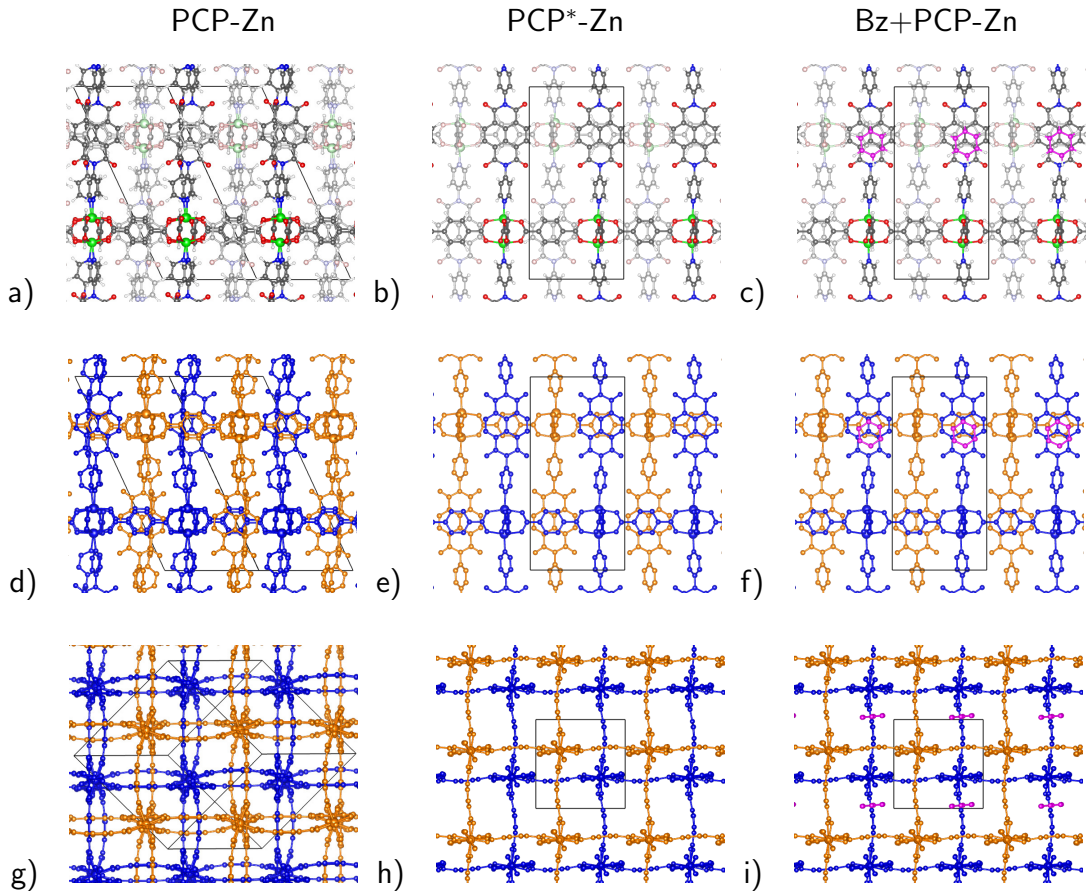

Figure 2. (a) PCP-Zn: Structure of pristine MOF before guest molecule introduction. (b) PCP*-Zn: Structure after guest-molecule induced structural change, but without guest molecule. (c) Bz+PCP-Zn: Structure after adsorption of benzene in the MOF. Atoms in (a)–(c) are colored as follows: C (grey), C_{Bz} (magenta), N (blue), O (red), Zn (green), and H (white). (d)–(f) are the same as (a)–(c), but here subframeworks are colored as blue (subframework 1) and orange (subframework 2) and the hydrogens are removed for clarity. (g)–(i) is a top view of (d)–(f).

change on the photoluminescence intensity without the benzene influence. The intensity of photoluminescence can be described by the oscillator strength between the HOMO and LUMO, Eq. (1). Figures S7a and S7b show the HOMO and LUMO of PCP-Zn and PCP*-Zn. The $\text{HOMO}_{\text{PCP-Zn}}$ is the bdc ligand and the metal nodes of both subframeworks while the $\text{LUMO}_{\text{PCP-Zn}}$ is the dpNDI ligand of both subframeworks. Those orbitals are delocalized and dispersed over both subframeworks throughout the PCP-Zn structure, which results in low oscillator strengths and henceforth photoluminescence. On the other hand, the $\text{HOMO}_{\text{PCP*-Zn}}$ is still the bdc ligand and metal node, but now both located on subframework 1, and the $\text{LUMO}_{\text{PCP*-Zn}}$ is the dpNDI of only subframework 2. Not only are $\text{HOMO}_{\text{PCP*-Zn}}$ and $\text{LUMO}_{\text{PCP*-Zn}}$ more localized but because of the structural change their distance is drastically reduced. While the HOMO and LUMO orbital character does not change between PCP-Zn and PCP*-Zn, the structural change decreases the orbital's spatial separation which, in turn, increases the oscillator strengths f_{ij} along the MD trajectory drastically, causing the significant increase in photoluminescence observed in Fig. 3.

The details of the benzene interaction will be discussed in the following section, but in order to understand why the structural change occurs upon adsorption, a look at how the benzene binds inside the MOF is helpful. In Bz+PCP-Zn, the benzene binds to the face of the dpNDI ligand but also faces the furthest facing bdc ligand, see Figs. 2c, 2f, and 2i. The introduction of benzene between the two aromatic ligands and the resulting π–π interactions cause a cross-linking and slight relative shift of the two subframeworks. One main question in this regard is whether the same effect—and the corresponding drastic increase in photoluminescence—can also be brought about by means other than introducing a guest molecule. To this end, we first analyze the energetics of the three structures in Fig. 4. As expected, PCP*-Zn is energetically unfavorable (albeit not by much), as the ground state of the empty MOF is known to be PCP-Zn. However, the energy penalty of the pure structure change from PCP-Zn to PCP*-Zn is overcome by the gain in binding energy upon the introduction of benzene, making Bz+PCP-Zn the new ground-state structure for the

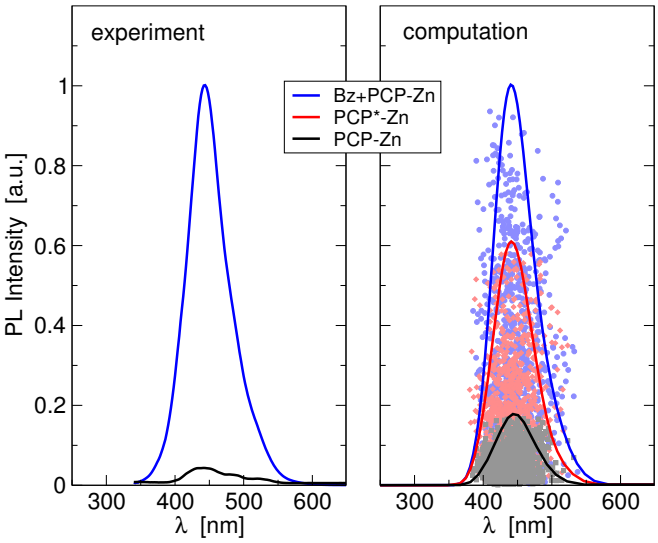

Figure 3. Photoluminescence spectrum for PCP-Zn (black) and Bz+PCP-Zn (blue). The transition from "off" to "on" in photoluminescence is clearly visible. The maximum of the Bz+PCP-Zn line is normalized to 1 in both panels. Results for the simulation of the artificial system PCP*-Zn (red) are also shown. The calculated f_{ij} values for the entire MD trajectory are plotted as faded symbols in the background and they are also plotted separately in Fig. S11.

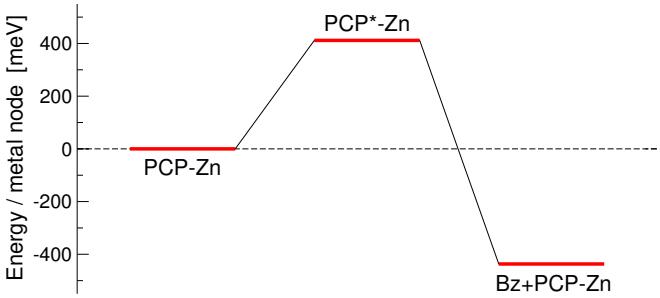

Figure 4. Schematic energy diagram for the energy per metal node of PCP*-Zn and Bz+PCP-Zn relative to PCP-Zn. Our simulations indicate that PCP*-Zn is (meta)stable.

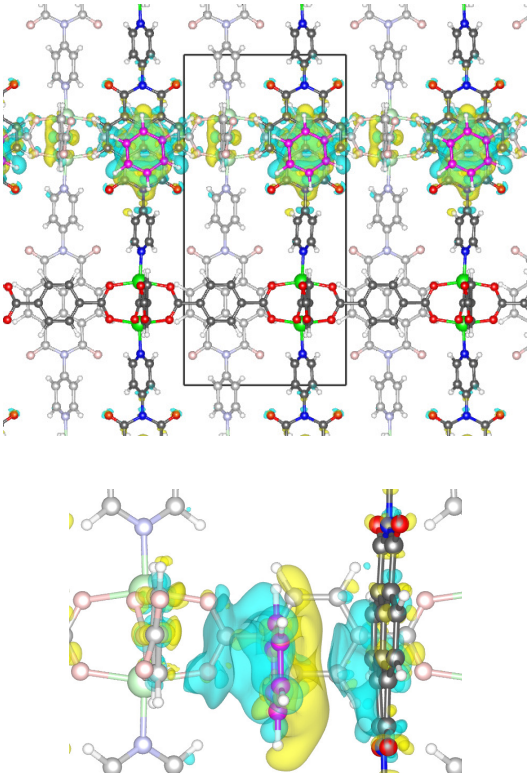

Figure 5. Induced charge rearrangement upon adsorption of benzene at an isosurface value of 2×10^{-4} $e/\text{Å}^3$. Yellow indicates a gain of charge and blue a loss of charge. Atoms are colored as follows: C (grey), C_{Bz} (magenta), N (blue), O (red), Zn (green), and H (white). The two subframeworks are depicted in bold and muted colors. The bottom panel is an enlarged side view of the top panel. Images without the isosurfaces and further, enlarged images can be found in Fig. S12.

loaded MOF. Analyzing the PCP*-Zn structure in more detail reveals that it is actually (meta)stable, evidenced by the following: (i) during our structural optimization of PCP*-Zn we saw no evidence that it wants to transform back to PCP-Zn.[51] (ii) We calculated the phonons of PCP*-Zn and found no imaginary frequencies. And (iii), we calculated the stress tensor of PCP*-Zn and found a change in the diagonal elements (related to pressure) and off-diagonal elements (related to shear) of only a few tenth of a kBar compared to Bz+PCP-Zn, close to the threshold of our accuracy. While all of those results suggest that PCP*-Zn is a (meta)stable structure, unfortunately, none of them can assess *how* stable the structure is. Even if it was stable enough to be observed experimentally, it is unclear how the structure could be accessed through experiment. Simply applying pressure to PCP-Zn will likely not result in PCP*-Zn, as the normalized unit-cell volume increases slightly when going from PCP-Zn to PCP*-Zn. Experimentally, we also tried outgassing a Bz+PCP-Zn sample under gentle conditions (vacuum at room temperature), but the corresponding PRXD spectra suggest that the outgassed structure returns to PCP-Zn.

B. Electronic Structure Induced Enhancement

When benzene adsorbs in the MOF, it not only causes the previously discussed structural change, but also further changes to the electronic structure. Our calculations show that benzene binds to PCP*-Zn with a binding energy of 849 meV, albeit what practically matters is the energy difference to the PCP-Zn structure, which is 437 meV (see Fig. 4). The benzene faces both the dp-NDI ligand (distance 3.62 Å) and bdc ligand (distance 3.69 Å). The adsorption of benzene in PCP*-Zn to arrive at Bz+PCP-Zn induces the charge rearrangement

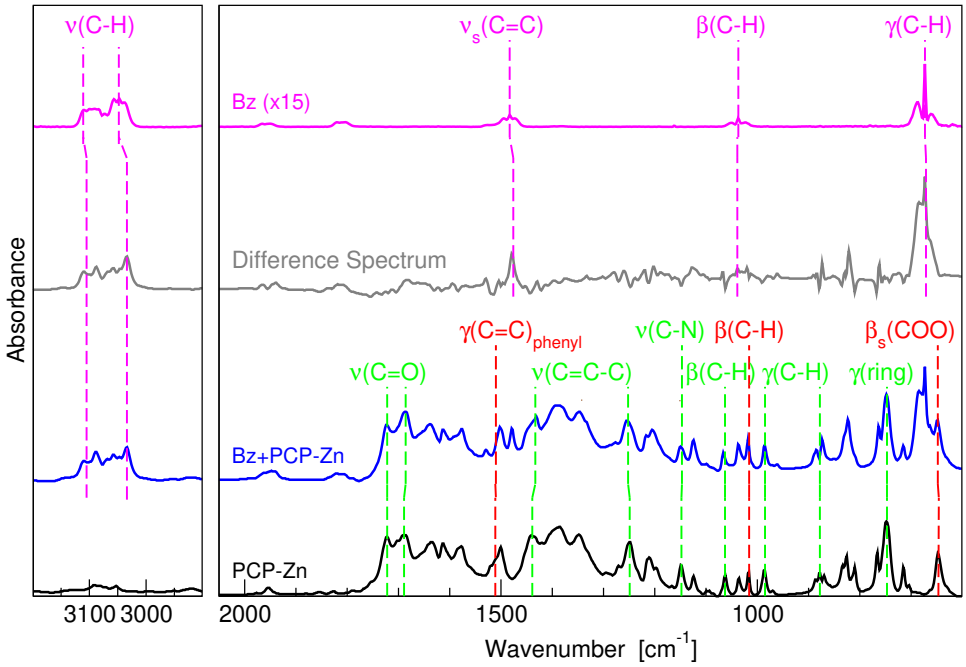

Figure 6. IR spectra of PCP-Zn (black), Bz+PCP-Zn (blue), their difference (grey), and benzene vapor-phase (magenta). Modes associated with the dpNDI ligand are identified with green dashed lines, the bdc ligand with red dashed lines, and the benzene with magenta dashed lines. Tables S1 and S2 give the wavenumbers of each mode along with the experimental/computational shift upon benzene adsorption. Modes are labeled as follows: ν refers to stretching, β is in plane bending, and γ is out of plane bending. Figures S8 and S9 show additional IR spectra of the ligands and benzene. Figures S13 and S14 show IR analyses for long-term and time-resolved Bz exposure, respectively.

depicted in Fig. 5, with charge gain on the face of benzene towards dpNDI and depletion on the face toward bdc. The strength of the interaction as well as the distance to the ligands and the small values in charge rearrangements are indicative of long-range van der Waals interactions. Figure S7 shows the HOMO and LUMO of the PCP-Zn, PCP*-Zn, and Bz+PCP-Zn systems using band decomposed charge densities. These orbitals are of the same ligand character for all three systems, i.e. the HOMOs are bdc orbitals and the LUMOs are a set of nearly energetically degenerate dpNDI orbitals with nearly the same shape.

However, as mentioned earlier, the $\text{HOMO}_{\text{PCP-Zn}}$ and the $\text{LUMO}_{\text{PCP-Zn}}$ are dispersed throughout both subframeworks with insignificant spatial separation. Going from PCP-Zn to PCP*-Zn, the accompanying structural change brings those orbitals closer together, leading to a significant increase of photoluminescence. Finally, adding the benzene now brings both the HOMO_{Bz} and LUMO_{Bz} onto the same subframework, bringing the orbitals yet closer together and leading to a further, albeit smaller, increase in photoluminescence. The benzene orbitals appear near the valence band edge of Bz+PCP-Zn at $\text{HOMO}_{\text{Bz}}^{-10}$, $\text{HOMO}_{\text{Bz}}^{-5}$, and $\text{HOMO}_{\text{Bz}}^{-4}$. Aside from the benzene orbitals in the valence band, all three studied structures have bdc orbitals near the valence band edge and dpNDI orbitals as the conduction band edge.

In order to confirm our computational model for the interactions involved in the benzene binding, *in situ* IR spectroscopic measurements were performed on PCP-Zn before and after *in situ* benzene vapor exposure. Additional spectra in the SI show the ligand contribution and benzene adsorption/desorption in Figs. S8 and S9, respectively. Figure 6 shows PCP-Zn, Bz+PCP-Zn, their difference, and benzene vapor-phase spectra. Shifts in Bz modes confirm that the Bz interacts with the PCP-Zn framework, listed in Table S2 and ranging from 0–14 cm^{-1}. Because Bz binds between both bdc and dpNDI ligands, it is likely that modes of both ligands are affected by the presence of the guest molecule. However, it is expected that dpNDI modes are more affected as there is clear charge gain between Bz and dpNDI when looking at the charge rearrangement induced by the Bz molecule (Fig. 5). Table S1 shows that some bdc modes are slightly shifted by 1–2 cm^{-1}, but the dpNDI modes do indeed have larger shifts, up to 6 cm^{-1}. The largest dpNDI shifts are identified in Fig. 6 along with the bdc shifts. Calculations of phonon mode shifts in Tables S1 and S2—induced by structural perturbations after benzene exposure—agree very well with our experimental shifts and support our model.

Calculated fluctuations of orbital energies along the MD trajectories are depicted in Fig. 7 and we find little difference between PCP-Zn, PCP*-Zn, and Bz+PCP-Zn. The only obvious difference is the added benzene orbitals for Bz+PCP-Zn in the valence band. Experimentally,

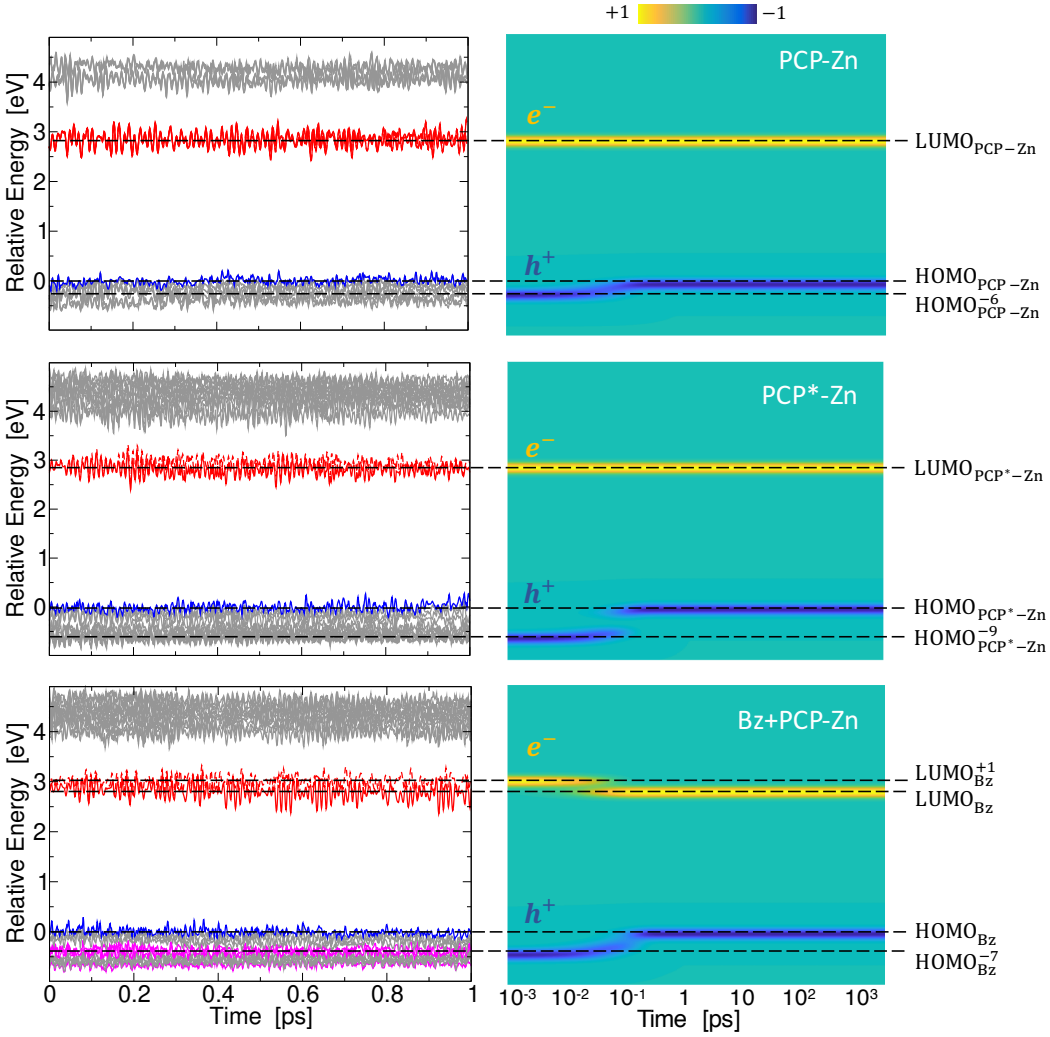

Figure 7. (left) Orbital energy fluctuation along the MD trajectory. The benzene molecule injects orbitals (magenta lines) below the valence band edge and the LUMO (red lines) as well as the HOMO (blue lines) are in essence identical for PCP-Zn, PCP*-Zn, and Bz+PCP-Zn. The LUMO orbitals are either energetically degenerate or nearly degenerate, indicated by corresponding red solid and dashed lines. Plots are aligned such that the timed-average of the HOMO energy is at zero. (right) Electron and hole relaxation after a 330 nm (3.76 eV) photoexcitation. Yellow indicates a gain of an electron, blue indicates a loss of an electron (i.e. hole), and green indicates no change in charge. Visualized orbitals for each structure can be found in Figs. S15, S16, and S17.

we find that PCP-Zn and Bz+PCP-Zn emit at the same wavelength, indicating that the band gaps are the same in both system. In addition, we study the electron and hole nonradiative relaxation in PCP-Zn, PCP*-Zn, and Bz+PCP-Zn in order to look at possible competing processes of radiative relaxation.[52] In general, if nonradiative relaxation of electrons and holes to the LUMO and HOMO, respectively, takes too long, photoluminescence (radiative relaxation) efficiency decreases. Experimentally, the studied excitation occurs at 330 nm (3.76 eV). We therefore analyze the transition with the highest oscillator strength (i.e. the most probably transition) near the 3.76 eV energy for each system. The various transitions are depicted in Fig. 7 and all originate deeper in the valence band and are excited to the conduction band edge, either the LUMO or one of the nearly energetically degenerate orbitals. In the case of Bz+PCP-Zn, the benzene slightly breaks the degeneracy and the electron is excited to $\mathrm{LUMO}^{+1}_{\mathrm{Bz}}$, but relaxes to the very close $\mathrm{LUMO}_{\mathrm{Bz}}$ on the 10^{-2} to 10^{-1} ps timescale. On the other hand, the benzene orbitals do not have an effect on the hole relaxation in the Bz+PCP-Zn. All systems have extremely fast relaxation for both electrons and holes, on the order of 10^{-2} to 10^{-1} ps, confirming that photoluminescence in these systems originates in LUMO to HOMO transitions on the much longer ns time scale. In particular, our results also show that the benzene guest molecule does not introduce any trap states (which would transfer charge to the guest) into the system. It is possible for such states to trap electrons and/or holes until photoluminescence

occurs eventually out of those trap states rather than the usual LUMO to HOMO transition. If the oscillator strengths for the trap-state transitions are larger and the trap states have large enough lifetimes, this provides a mechanism for photoluminescence enhancement,[28] but this is clearly not the case here.

The electron/hole relaxation pathways through the MOF in real-space are depicted in Fig. S10. The PCP*-Zn and Bz+PCP-Zn systems show a clear relaxation with time for both the electron and hole. Because of the dispersed nature of the PCP-Zn orbitals around the band edge, the relaxation in this system is not immediately obvious but is noted by the change in *intensity* for the hole and electron around 10^{-2} ps. Even though the PCP-Zn electron and hole are dispersed throughout the framework compared to the much more localized PCP*-Zn and Bz+PCP-Zn cases, the relaxation rates are not significantly affected by the delocalization.

IV. CONCLUSIONS

The photoluminescent sensing MOF PCP-Zn is essentially photo-inactive in its pristine/empty state. However, upon adsorption of aromatic guest molecules a structural change is induced and the system now strongly luminesces. While the guest molecule does also induce electronic structure changes, we show that the structural change is the main driving force for this "turn on" mechanism. Furthermore, we uncover the reason for the photo-inactivity of PCP-Zn to be its interpenetrated structure. The $\mathrm{HOMO}_{\mathrm{PCP\text{-}Zn}}$ and $\mathrm{LUMO}_{\mathrm{PCP\text{-}Zn}}$ are located on separate subframeworks, which increases their distance and, in turn, oscillator strengths. On the other hand, a subframework alignment and structural change significantly decrease the distance between $\mathrm{HOMO}_{\mathrm{PCP^*\text{-}Zn}}$ and $\mathrm{LUMO}_{\mathrm{PCP^*\text{-}Zn}}$, increasing the oscillator strengths and explaining a large portion of the observed photoluminescence enhancement. The actual inclusion of the aromatic guest molecules is then responsible for more subtle changes in the electronic structure, leading to a further, smaller enhancement of the photoluminescence. While we were able to disentangle the overall enhancement into a major structural and a minor electronic-structure contribution via our simulations, the tantalizing question remains if those two mechanisms can be separated in practice and if the structural change with its corresponding enhancement of photoluminescence can be brought about by means other than the adsorption of guest molecules.

ACKNOWLEDGMENTS

This work was entirely supported by the U. S. Department of Energy, Office of Science, Office of Basic Energy Sciences; it started under Award No. DE-FG02-08ER46491 and finished under Award No. DE-SC0019902.

SUPPORTING INFORMATION

Discussions: computational approximations; calculating oscillator strength; calculating nonadiabatic coupling; calculating Huang-Rhys factors; calculating thermal ellipsoids; synthesis of dpNDI ligand; and stability of pressing PCP-Zn on KBr pellets.

Tables: IR modes of ligands and benzene.

Figures: HNMR of dpNDI; Analysis of PCP-Zn pressed on KBr pellet (PXRD, micrscopic imaging, and Raman); PXRD of PCP-Zn, outgassed PCP-Zn, and Bz+PCP-Zn; calculated thermal ellipsoids of PCP-Zn and Bz+PCP-Zn; band decomposed charge density of PCP-Zn, PCP*-Zn, and Bz+PCP-Zn; IR spectra of ligands and PCP-Zn; IR spectra of PCP-Zn, Bz+PCP-Zn difference spectra with evacuation; Real-space electron and hole relaxation; Calculated oscillator strength of PCP-Zn, PCP*-Zn, and Bz+PCP-Zn; enlarged images of Bz in PCP-Zn; IR spectra of long term Bz exposure in PCP-Zn; Time resolved IR of Bz in PCP-Zn; Partial charge densities of PCP-Zn, PCP*-Zn, and Bz+PCP-Zn.

* E-mail: thonhauser@wfu.edu

[1] Liu, J.; Thallapally, P. K.; McGrail, B. P.; Brown, D. R.; Liu, J. Progress in adsorption-based CO_2 capture by metal-organic frameworks. *Chem. Soc. Rev.* **2012**, *41*, 2308–2322.

[2] Murray, L. J.; Dinca, M.; Long, J. R. Hydrogen storage in metal-organic frameworks. *Chem. Soc. Rev.* **2009**, *38*, 1294–1314.

[3] Li, J.-R.; Ma, Y.; McCarthy, M. C.; Sculley, J.; Yu, J.; Jeong, H.-K.; Balbuena, P. B.; Zhou, H.-C. Carbon dioxide capture-related gas adsorption and separation in metal-organic frameworks. *Coord. Chem. Rev.* **2011**, *255*, 1791–1823.

[4] Nijem, N.; Wu, H.; Canepa, P.; Marti, A.; Balkus, K. J.; Thonhauser, T.; Li, J.; Chabal, Y. J. Tuning the gate opening pressure of metal-organic frameworks (MOFs) for the selective separation of hydrocarbons. *J. Am. Chem. Soc.* **2012**, *134*, 15201–15204.

[5] Lee, K.; Howe, J. D.; Lin, L.-C.; Smit, B.; Neaton, J. B. Small-molecule adsorption in open-site metal-organic frameworks: A systematic density functional theory study for rational design. *Chem. Mater.* **2015**, *27*, 668–678.

[6] Zhao, D.; Yuan, D.; Zhou, H.-C. The current status of hydrogen storage in metal-organic frameworks. *Energy Environ. Sci.* **2008**, *1*, 222–235.

[7] Rosi, N. L.; Eckert, J.; Eddaoudi, M.; Vodak, D. T.; Kim, J.; O'Keeffe, M.; Yaghi, O. M. Hydrogen storage in microporous metal-organic frameworks. *Science* **2003**, *300*, 1127–1129.

[8] Wu, H.; Gong, Q.; Olson, D. H.; Li, J. Commensurate adsorption of hydrocarbons and alcohols in microporous metal organic frameworks. *Chem. Rev.* **2012**, *112*, 836–868.

[9] He, Y.; Zhou, W.; Qian, G.; Chen, B. Methane storage in metal-organic frameworks. *Chem. Soc. Rev.* **2014**, *43*, 5657–5678.

[10] Wu, C.-D.; Lin, W. Heterogeneous asymmetric catalysis with homochiral metal-organic frameworks: Network-structure-dependent catalytic activity. *Angew. Chem. Int. Ed.* **2007**, *46*, 1075–1078.

[11] Lee, J.; Farha, O. K.; Roberts, J.; Scheidt, K. A.; Nguyen, S. T.; Hupp, J. T. Metal-organic framework materials as catalysts. *Chem. Soc. Rev.* **2009**, *38*, 1450–1459.

[12] Zou, R.-Q.; Sakurai, H.; Xu, Q. Preparation, adsorption properties, and catalytic activity of 3D porous metal-organic frameworks composed of cubic building blocks and alkali-metal ions. *Angew. Chem. Int. Ed.* **2006**, *45*, 2542–2546.

[13] Luz, I.; Llabrés i Xamena, F. X.; Corma, A. Bridging homogeneous and heterogeneous catalysis with MOFs: "Clic" reactions with Cu-MOF catalysts. *J. Catal.* **2010**, *276*, 134–140.

[14] Uemura, T.; Yanai, N.; Kitagawa, S. Polymerization reactions in porous coordination polymers. *Chem. Soc. Rev.* **2009**, *38*, 1228–1236.

[15] Vitorino, M. J.; Devic, T.; Tromp, M.; Férey, G.; Visseaux, M. Lanthanide metal organic frameworks as Ziegler-Natta catalysts for the selective polymerization of isoprene. *Macromol. Chem. Phys.* **2009**, *210*, 1923–1932.

[16] Liu, Y.; Kabbour, H.; Brown, C. M.; Neumann, D. A.; Ahn, C. C. Increasing the density of adsorbed hydrogen with coordinatively unsaturated metal centers in metal-organic frameworks. *Langmuir* **2008**, *24*, 4772–4777.

[17] Zhou, W.; Wu, H.; Yildirim, T. Enhanced H_2 adsorption in isostructural metal-organic frameworks with open metal sites: Strong dependence of the binding strength on metal ions. *J. Am. Chem. Soc.* **2008**, *130*, 15268–15269.

[18] Wu, H.; Zhou, W.; Yildirim, T. High-capacity methane storage in metal-organic frameworks M_2(dhtp): The important role of open metal sites. *J. Am. Chem. Soc.* **2009**, *131*, 4995–5000.

[19] Bordiga, S.; Lamberti, C.; Ricchiardi, G.; Regli, L.; Bonino, F.; Damin, A.; Lillerud, K.-P.; Bjorgen, M.; Zecchina, A. Electronic and vibrational properties of a MOF-5 metal-organic framework: ZnO quantum dot behaviour. *Chem. Commun.* **2004**, 2300–2301.

[20] Stroppa, A.; Jain, P.; Barone, P.; Marsman, M.; Perez-Mato, J. M.; Cheetham, A. K. K.; Kroto, H. W.; Picozzi, S. Electric control of magnetization and interplay between orbital ordering and ferroelectricity in a multiferroic metal organic framework. *Angew. Chem. Int. Ed.* **2011**, *50*, 5847–5850.

[21] Stroppa, A.; Barone, P.; Jain, P.; Perez-Mato, J. M.; Picozzi, S. Hybrid improper ferroelectricity in a multiferroic and magnetoelectric metal organic framework. *Adv. Mater.* **2013**, *25*, 2284–2290.

[22] Di Sante, D.; Stroppa, A.; Jain, P.; Picozzi, S. Tuning the ferroelectric polarization in a multiferroic metal-organic framework. *J. Am. Chem. Soc.* **2013**, *135*, 18126–18130.

[23] Horcajada, P. et al. Porous metal-organic-framework nanoscale carriers as a potential platform for drug delivery and imaging. *Nat. Mater.* **2010**, *9*, 172.

[24] Allendorf, M. D.; Bauer, C. A.; Bhakta, R. K.; Houk, R. Luminescent metal organic frameworks. *Chem. Soc. Rev.* **2009**, *38*, 1330–1352.

[25] White, K. A.; Chengelis, D. A.; Gogick, K. A.; Stehman, J.; Rosi, N. L.; Petoud, S. Near-infrared luminescent lanthanide MOF barcodes. *J. Am. Chem. Soc.* **2009**, *131*, 18069–18071.

[26] Miller, S. E.; Teplensky, M. H.; Moghadam, P. Z.; Fairen-Jimenez, D. Metal-organic frameworks as biosensors for luminescence-based detection and imaging. *Interface Focus* **2016**, *6*, 20160027.

[27] Canepa, P.; Tan, K.; Du, Y.; Lu, H.; Chabal, Y. J.; Thonhauser, T. Structural, elastic, thermal, and electronic responses of small-molecule-loaded metal-organic framework materials. *J. Mater. Chem. A* **2015**, *3*, 986–995.

[28] Kreno, L. E.; Leong, K.; Farha, O. K.; Allendorf, M.; Van Duyne, R. P.; Hupp, J. T. Metal-organic framework materials as chemical sensors. *Chem. Rev.* **2012**, *112*, 1105–1125.

[29] Serre, C.; Mellot-Draznieks, C.; Surblé, S.; Audebrand, N.; Filinchuck, Y.; Férey, G. Role of solvent-host interactions that lead to very large swelling of hybrid frameworks. *Science* **2007**, *315*, 1828–1831.

[30] Allendorf, M. D.; Houk, R. J. T.; Andruskiewicz, L.; Talin, A. A.; Pikarsky, J.; Choundhury, A.; Gall, K. A.; Hensketh, P. J. Stress-induced chemical detection using flexible metal-organic frameworks. *J. Am. Chem. Soc.* **2008**, *130*, 14404.

[31] Tan, J.-C.; Cheetham, A. K. Mechanical properties of hybrid inorganic-organic framework materials: Establishing fundamental structure-property relationships. *Chem. Soc. Rev.* **2011**, *40*, 1059–1080.

[32] Hu, Z.; Deibert, B. J.; Li, J. Luminescent metal-organic frameworks for chemical sensing and explosive detection. *Chem. Soc. Rev.* **2014**, *43*, 5815–5840.

[33] Lin, R.-B.; Liu, S.-Y.; Ye, J.-W.; Li, X.-Y.; Zhang, J.-P. Photoluminescent metal–organic frameworks for gas sensing. *Adv. Sci.* **2016**, *3*, 1500434.

[34] Lustig, W. P.; Mukherjee, S.; Rudd, N. D.; Desai, A. V.; Li, J.; Ghosh, S. K. Metal–organic frameworks: Functional luminescent and photonic materials for sensing applications. *Chem. Soc. Rev.* **2017**, *46*, 3242–3285.

[35] Yu, Y.; Ma, J.-P.; Dong, Y.-B. Luminescent humidity sensors based on porous Ln^{3+}-MOFs. *CrystEngComm* **2012**, *14*, 7157–7160.

[36] Harbuzaru, B. V.; Corma, A.; Rey, F.; Jordá, J. L.; Ananias, D.; Carlos, L. D.; Rocha, J. A miniaturized linear pH sensor based on a highly photoluminescent self-assembled europium (III) metal–organic framework. *Angew. Chem.* **2009**, *48*, 6476–6479.

[37] Ma, D.; Li, B.; Zhou, X.; Zhou, Q.; Liu, K.; Zeng, G.; Li, G.; Shi, Z.; Feng, S. A dual functional MOF as a luminescent sensor for quantitatively detecting the concentration of nitrobenzene and temperature. *ChemComm* **2013**, *49*, 8964–8966.

[38] Müller-Buschbaum, K.; Beuerle, F.; Feldmann, C. MOF based luminescence tuning and chemical/physical sensing. *Micropor. Mesopor. Mat.* **2015**, *216*, 171–199.

[39] Pramanik, S.; Zheng, C.; Zhang, X.; Emge, T. J.; Li, J. New microporous metal–organic framework demonstrating unique selectivity for detection of high explosives and aromatic compounds. *J. Am. Chem. Soc.* **2011**, *133*, 4153–4155.

[40] Hu, Z.; Tan, K.; Lustig, W. P.; Wang, H.; Zhao, Y.; Zheng, C.; Banerjee, D.; Emge, T. J.; Chabal, Y. J.; Li, J. Effective sensing of RDX via instant and selective detection of ketone vapors. *Chem. Sci.* **2014**, *5*, 4873–4877.

[41] Takashima, Y.; Martínez, V. M.; Furukawa, S.; Kondo, M.; Shimomura, S.; Uehara, H.; Nakahama, M.; Sugimoto, K.; Kitagawa, S. Molecular decoding using luminescence from an entangled porous framework. *Nat. Comm.* **2011**, *2*, 168.

[42] Kresse, G.; Furthmüller, J. Efficient iterative schemes for ab initio total-energy calculations using a plane-wave basis set. *Phys. Rev. B* **1996**, *54*, 11169–11186.

[43] Kresse, G.; Joubert, D. From ultrasoft pseudopotentials to the projector augmented-wave method. *Phys. Rev. B* **1999**, *59*, 1758–1775.

[44] Berland, K.; Cooper, V. R.; Lee, K.; Schröder, E.; Thonhauser, T.; Hyldgaard, P.; Lundqvist, B. I. Van der Waals forces in density functional theory: A review of the vdW-DF method. *Reports Prog. Phys.* **2015**, *78*, 066501.

[45] Langreth, D. C. et al. A density functional for sparse matter. *J. Phys. Condens. Matter* **2009**, *21*, 084203.

[46] Thonhauser, T.; Cooper, V. R.; Li, S.; Puzder, A.; Hyldgaard, P.; Langreth, D. C. Van der Waals density functional: Self-consistent potential and the nature of the van der Waals bond. *Phys. Rev. B* **2007**, *76*, 125112.

[47] Thonhauser, T.; Zuluaga, S.; Arter, C. A.; Berland, K.; Schröder, E.; Hyldgaard, P. Spin signature of nonlocal correlation binding in metal-organic frameworks. *Phys. Rev. Lett.* **2015**, *115*, 136402.

[48] Jensen, S.; Tan, K.; Lustig, W.; Kilin, D.; Li, J.; Chabal, Y.; Thonhauser, T. Quenching of photoluminescence in a Zn-MOF sensor by nitroaromatic molecules. *J. Mater. Chem. C* **2019**, *7*, 2625–2632.

[49] Kasha, M. Characterization of electronic transitions in complex molecules. *Discuss. Faraday Soc.* **1950**, *9*, 14–19.

[50] Mukherjee, S.; Babarao, R.; Desai, A. V.; Manna, B.; Ghosh, S. K. Polar pore surface guided selective CO_2 adsorption in a prefunctionalized metal–organic framework. *Cryst. Growth Des.* **2017**, *17*, 3581–3587.

[51] The structural optimization of PCP*-Zn was done in two ways. First, we started from Bz+PCP-Zn and removed the benzene, followed by an optimization of the unit cell parameters and atom position; only minor changes were found. Second, we represented PCP*-Zn in the twice-as-large unit cell of PCP-Zn and again optimization only led to minor changes.

[52] Lakowicz, J. *Principles of fluorescence spectroscopy*, 3rd ed.; Springer, 2006; p 10.

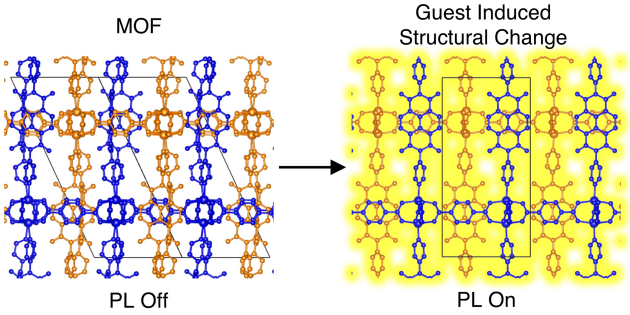

Figure 8. TOC Figure

— Supplementary Information —

Structure-Driven Photoluminescence Enhancement in a Zn-based Metal Organic Framework

Stephanie Jensen,[1,2] Kui Tan,[3] William P. Lustig,[4] Dmitri S. Kilin,[5] Jing Li,[4] Yves J. Chabal,[3] and Timo Thonhauser[1,2,*]

[1] *Department of Physics, Wake Forest University, Winston-Salem, NC 27109, USA*
[2] *Center for Functional Materials, Wake Forest University, Winston-Salem, NC 27109, USA*
[3] *Department of Materials Science and Engineering, University of Texas at Dallas, Richardson, TX 75080, USA*
[4] *Department of Chemistry and Chemical Biology, Rutgers University, Piscataway, NJ 08854, USA*
[5] *Department of Chemistry and Biochemistry, North Dakota State University, Fargo, ND 58108, USA*

(Dated: September 6, 2019)

I. COMPUTATIONAL DETAILS

A. Approximations

Two main hypotheses are used in order to model the experimental photoluminescence in MOFs. Kasha's rule[1] tells us that the lowest excitation, from LUMO to HOMO, will be the only transition which exhibits luminescence with substantial yield. Additionally, photoluminescent linewidth broadening occurs because ions are constantly moving and reorganizing. This means that we need calculations beyond the ground state. Here, we make two approximations in order to calculate the optical properties: the independent orbital approximation, where the transition probability is calculated between two specified states, and the dipole approximation, where we assume that the electromagnetic wavelength is much larger than the length of the molecular system.

B. Oscillator Strength

The oscillator strengths f_{ij} between states i and j are sampled along the nuclear trajectory $\{\mathbf{R}_\mathrm{I}(t)\}$ in order to obtain the optical properties. The transitions run over the occupied states i (592 in PCP-Zn, 296 in PCP*-Zn, and 311 in Bz+PCP-Zn) and the unoccupied states j (176 in PCP-Zn, 82 in PCP*-Zn, and 97 in Bz+PCP-Zn). The standard VASP *ab initio* Verlet algorithm with total free-energy conservation is used to get a 1000 time step molecular dynamics (MD) trajectory, totaling 1 ps. The photoluminescence spectra are then calculated from the LUMO to HOMO transition, overlaying a Gaussian, and summing over all time steps of the trajectory.

Equation (1) in the main manuscript shows that the oscillator strengths f_{ij} depend on the orbitals i (occupied) and j (unoccupied) and their energy difference. Even though DFT does not accurately capture the energy difference between such states, the shape of the Kohn-Sham (KS) orbitals ψ_i^KS and ψ_j^KS is relatively accurate. As a result, the $\mathbf{D}_{ij}$ values in Eq. (2) in the main manuscript are meaningful. GW calculations were attempted to better assess the energy differences across the band gap, but the unit cells are too large for this level of calculation. Therefore, we calculate $\mathbf{D}_{ij}$ at the KS level and for f_{ij} the "scissors" operator is implemented as a post-processing step. This operator adjusts the KS band gap to our experimentally measured one. Further details and justification for this approach can be found in Ref. [2].

C. Nonadiabatic Coupling Relaxation Dynamics

Non-adiabatic electronic couplings and, in turn, the non-radiative lifetime of the excited state electron and hole can also be calculated from the MD trajectory. These calculations go beyond the Born-Oppenheimer approximation—which treats nuclear motion and electronic structure separately—by looking at the electronic response to nuclear reorganization. Kinetic energy is kept constant by interfacing the MD with a thermostat. The on-the-fly non-adiabatic couplings are computed as

$$\mathbf{V}_{ij}^\mathrm{NA}(t) = -\frac{i\hbar}{2\Delta t}\int \psi_i^*\big(\{\mathbf{R}_\mathrm{I}(t)\}\big)\ \psi_j\big(\{\mathbf{R}_\mathrm{I}(t+\Delta t)\}\big)\ d^3r\ . \quad (1)$$

$\mathbf{V}_{ij}^\mathrm{NA}(t)$ serves as a measure of electron-phonon coupling, which is used for calculating the relaxation rates and dynamics, with details found elsewhere.[3,4] The 10^{-2} to 10^{-1} ps timescale found in the main manuscript for electron and hole relaxation to the LUMO and HOMO, respectively, provides *a posteriori* reasoning for only using the LUMO to HOMO transition to describe photoluminescence, known to occur on a ns timescale. Additional details can be found in our prior work.[2]

D. Huang-Rhys Factor

We make the approximation that the ground-state MD trajectory adequately describes the excited states. To

support this approximation, a mean displacement measure, the Huang-Rhys factor D, must be less than one but ideally close to zero. A value of zero means that the excited-state ionic structure is the same as the one for the ground state. To measure D, an electron is excited from HOMO to LUMO and relaxed, giving the excited state geometry. By projecting this geometry onto the phonon modes of the system (with the best match chosen), we find the displacement d of the most perturbed atom, the reduced mass $m = m_1 m_2/(m_1 + m_2)$ (m_1 is the mass of the most perturbed atom and m_2 is the mass of its nearest neighbor), and ω_0 (the angular frequency of the phonon mode). D is then calculated as $D = d^2 m\omega_0/2\hbar$. We find $D = 0.17$ for Bz+PCP-Zn, which we use for all three models as the PCP-Zn unit cell is much larger, the PCP*-Zn structure is similar to that of Bz+PCP-Zn, and the benzene orbitals are not involved in the excitation.

E. Thermal Ellipsoids

The mean square displacement matrix, $\mathbf{U}$, describes the vibrations of ions during the MD trajectory, allowing us to create thermal ellipsoid images.[5] The matrix elements are defined as $U_{\alpha\beta} = \left\langle (u_\alpha - \bar{u}_\alpha)(u_\beta - \bar{u}_\beta) \right\rangle$, where α and β are coordinate axes and $\bar{u}_\alpha$ is the average position along the α axis. The values are calculated for every atom along the x, y, and z axes using the position of the atoms at each time step of the MD trajectory.

II. SYNTHESIS OF dpNDI

1.86 mmol of 1,4,5,8-naphthalenetetracarboxylic dianhydride was combined with 4.48 mmol of 4-aminopyridine in 20 mL dry dimethylformamide (DMF) under nitrogen and refluxed at 130 °C for eight hours. The reaction was then allowed to cool to room temperature, precipitating the impure ligand dpNDI, which was filtered out and recrystallized in DMF. The ligand was then washed with cold 50:50 CH_2Cl_2:acetone and dried under vacuum at 40 °C overnight to give the pure dpNDI in 67% yield.

III. STABILITY OF KBr PELLETS

Pellet pressing is a common sample preparation technique for performing transmission IR measurements. While this technique could break the large crystallites, the microscopic crystalline structure is usually preserved as we have demonstrated in our XRD, optical imaging, and Raman measurement. The PXRD measurements of MOF powders pressed onto KBr pellets were carried out before and after activation at 150 °C. The corresponding results presented in Fig. S2a show that most peaks are retained but exhibit some broadening compared with the patterns of the outgassed MOF powder in its pristine form (before pressing on KBr). Pressing can cause the large crystallites to break into small pieces (see Fig. S2b), which accounts for the broadening of PXRD peaks. In addition, the extra peak at 9° shows the existence of the as-made phase. After activation at 150 °C, this peak disappeared, indicating that the as-made phase is completely transformed into the outgassed phase. Moreover, all the peaks show further broadening suggesting that crystallites downsize upon annealing. To further examine chemical stability of the PCP powder and microscopic changes occurring in the crystallites, Raman spectra were taken on the sample in its powder form and on the KBr pellet before and after activation. Neither loss of MOF phonon modes (including the stretching of COO that connects the metal node) nor the appearance of new peaks were detected, indicating that PCP samples do not suffer chemical decomposition but retain its microcrystalline structure.

IV. ADDITIONAL TABLES AND FIGURES

Mode	PCP-Zn [cm^{-1}]	Bz+PCP-Zn [cm^{-1}]	Exp. Shift [cm^{-1}]	Calc. Shift [cm^{-1}]
dpNDI				
ν(C=O)	1722	1722	0	0
ν(C=O)	1689	1686	3	3
ν(C=C–C)	1439	1433	6	4
ν(C=C–C)	1249	1252	−3	−4
ν(C–N)	1148	1147	1	1
β(C–H)	1063	1063	0	1
γ(C–H)	985	985	0	0
γ(C–H)	878	878	0	0
γ(ring bend)	747	747	0	0
bdc				
$\nu(\text{C=C})_{\text{phenyl}}$	1511	1510	1	1
β(C–H)	1016	1016	0	0
β_s(COO)	647	647	0	0

Table S1. Assigned experimental IR modes, identified in Fig. 6 of the main manuscript, along with their experimental and calculated shifts. Excellent agreement is found between experiment and theory, validating our model and showing that benzene is bound into PCP-Zn. Figure S8 shows the bdc and dpNDI ligand mode shifts in reference to PCP-Zn. Modes are labeled as follows: ν refers to stretching, β is in-plane bending, and γ is out-of-plane bending.

Mode	vapor-phase benzene [cm^{-1}]	Bz+PCP-Zn [cm^{-1}]	Exp. Shift [cm^{-1}]	Calc. Shift [cm^{-1}]
ν(CH)	3111	3105	6	5
ν(CH)	3048	3034	14	17
ν_s(C=C)	1483	1476	7	7
β (CH)	1037	1039	−2	0
ν(CH)	673	671	2	3

Table S2. Assigned experimental IR modes of benzene in vapor-phase and Bz+PCP-Zn along with their experimental and calculated shifts. These modes are identified in Fig. 6 of the main manuscript and Fig. S9. Modes are labeled as follows: ν refers to stretching and β is in-plane bending.

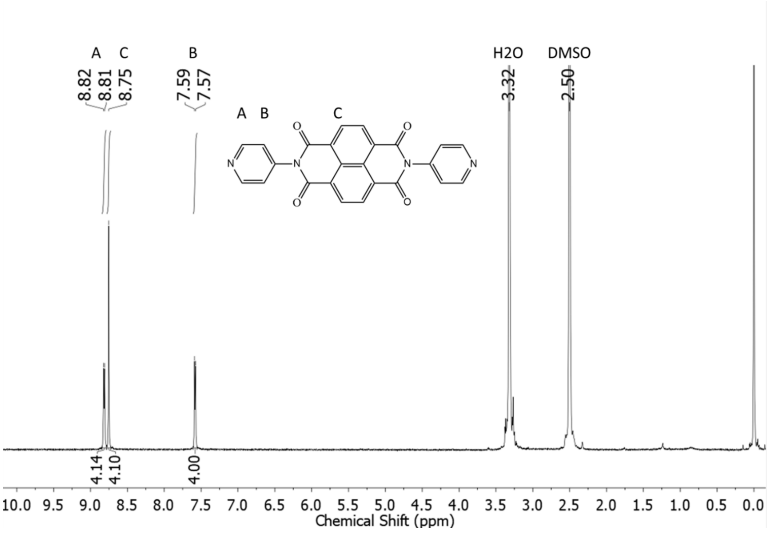

Figure S1. ^{1}H NMR of the dpNDI ligand (400 MHz, DMSO-d6) δ 8.82 (d, 4H, J = 6.0 Hz), 8.75 (s, 4H), 7.58 (d, 4H, J = 6.0 Hz).

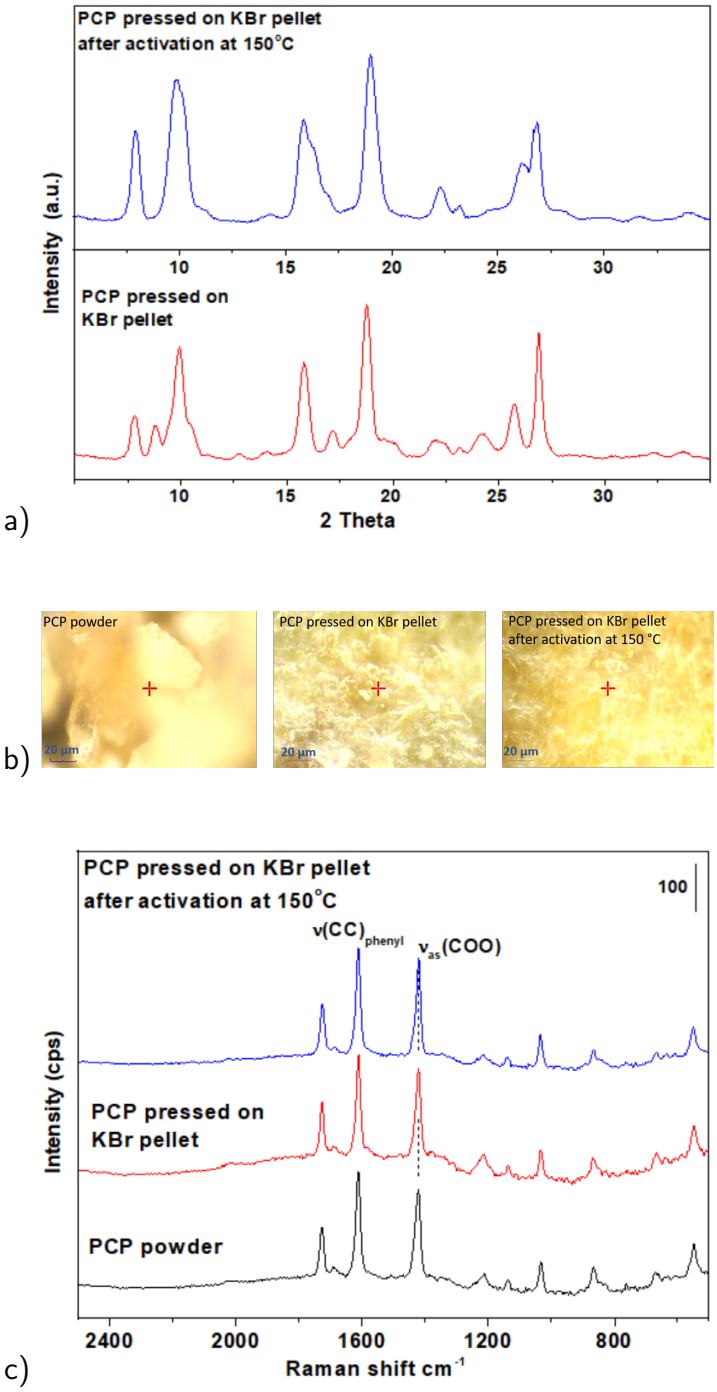

Figure S2. Analysis of PCP-Zn upon pressing on a KBr pellet and activating to 150 °C. a) Powder X-ray diffraction patterns of PCP-Zn samples, b) microscopic image of PCP-Zn crystallites, c) Raman spectra of PCP-Zn samples.

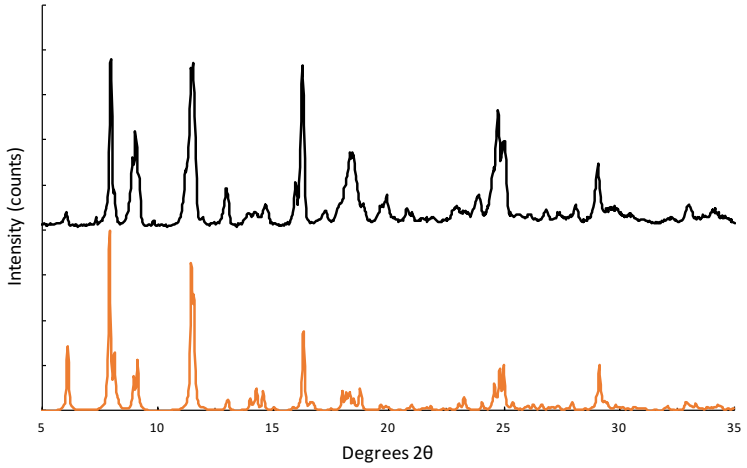

Figure S3. Powder X-ray diffraction (PXRD) pattern for the as-made PCP-Zn (black) overlaid on the simulated PXRD pattern of the as-made PCP-Zn (orange).

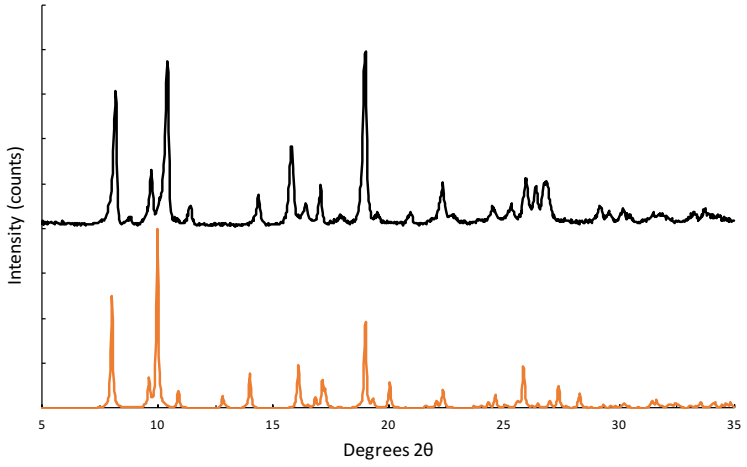

Figure S4. PXRD pattern for the outgassed PCP-Zn (black) overlaid on the simulated PXRD pattern of the outgassed PCP-Zn (orange).

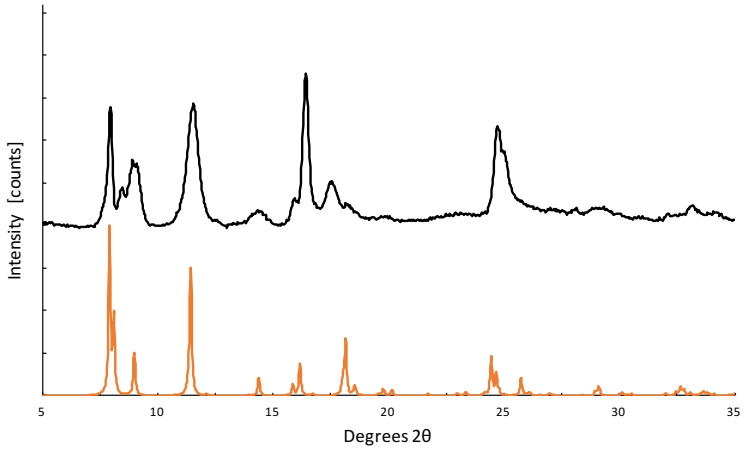

Figure S5. PXRD patterns for the benzene-loaded Bz+PCP-Zn (black, after 10 days of Bz exposure) overlaid on the simulated PXRD pattern of the solvated Bz+PCP-Zn (orange).

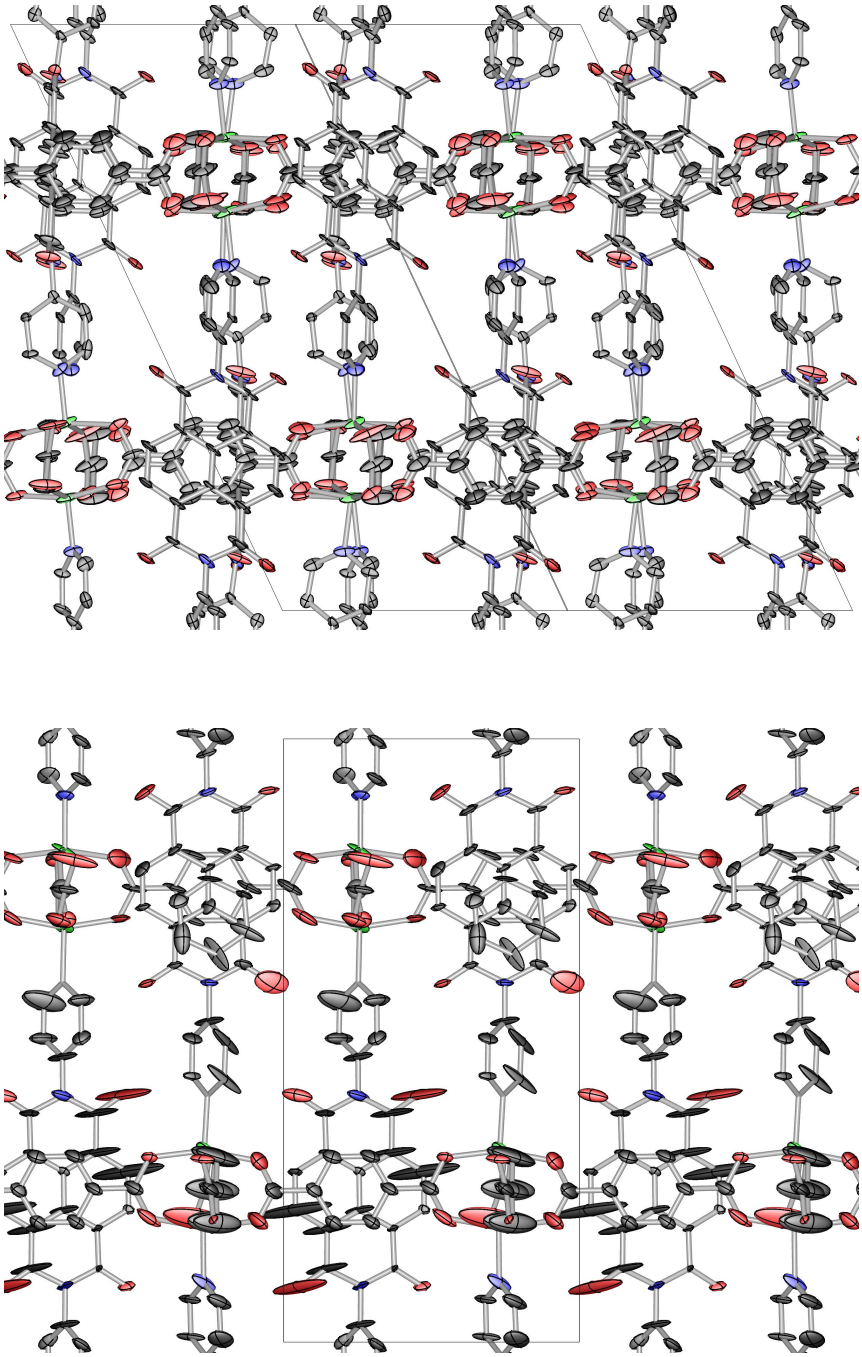

Figure S6. Thermal ellipsoid images of PCP-Zn (top) and Bz+PCP-Zn (bottom) at the 99% probability level for $T = 300$ K. The variance $\mathbf{U}$ was calculated as outlined in Sec. I E. For clarity, thermal ellipsoids for hydrogen are not depicted.

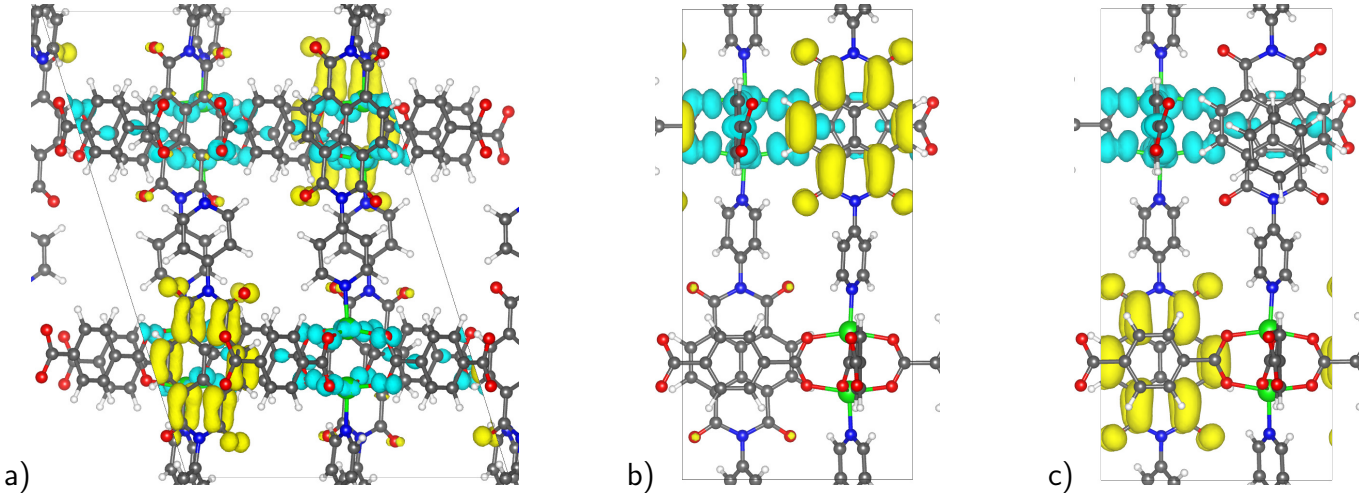

Figure S7. Band decomposed charge density images of a) PCP-Zn, b) PCP*-Zn, and c) Bz+PCP-Zn. The HOMO is shown in blue and the LUMO is depicted in yellow, both at an isosurface value of 2×10^{-3} $e/\text{Å}^3$. The structural change from PCP-Zn to PCP*-Zn shifts the HOMO and LUMO from being dispersed and far apart to localized and much closer together. The actual adsorption of the benzene guest molecule in Bz+PCP-Zn then shifts the HOMO and LUMO even closer and onto the same subframework, resulting in a further increase of the oscillator strengths and enhancement of the photoluminescence.

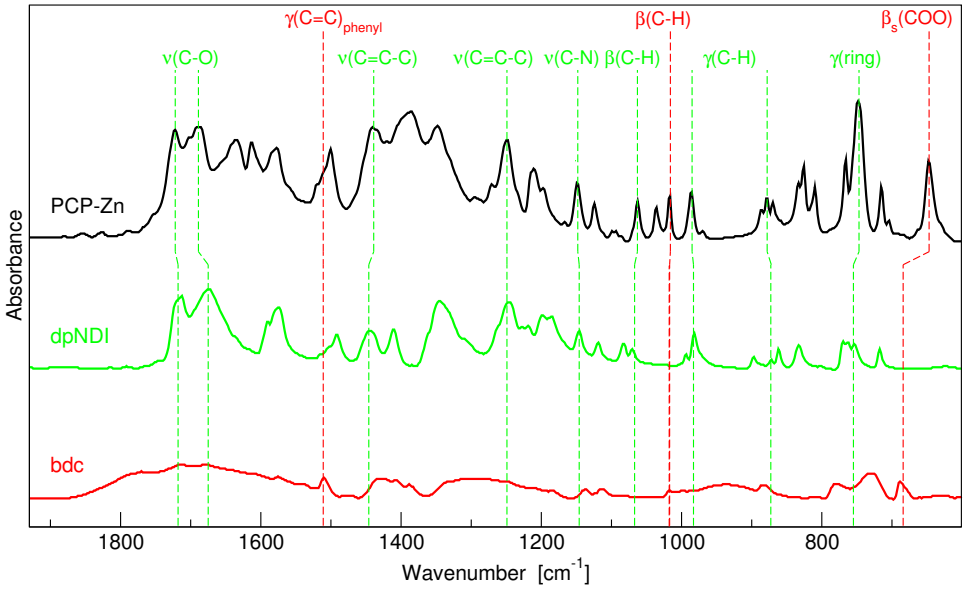

Figure S8. IR spectra of the bdc (red) and dpNDI (green) ligands along with PCP-Zn (black). The PCP-Zn IR spectrum is dominated by dpNDI peaks. Modes are labeled as follows: ν refers to stretching, β is in-plane bending, and γ is out-of-plane bending.

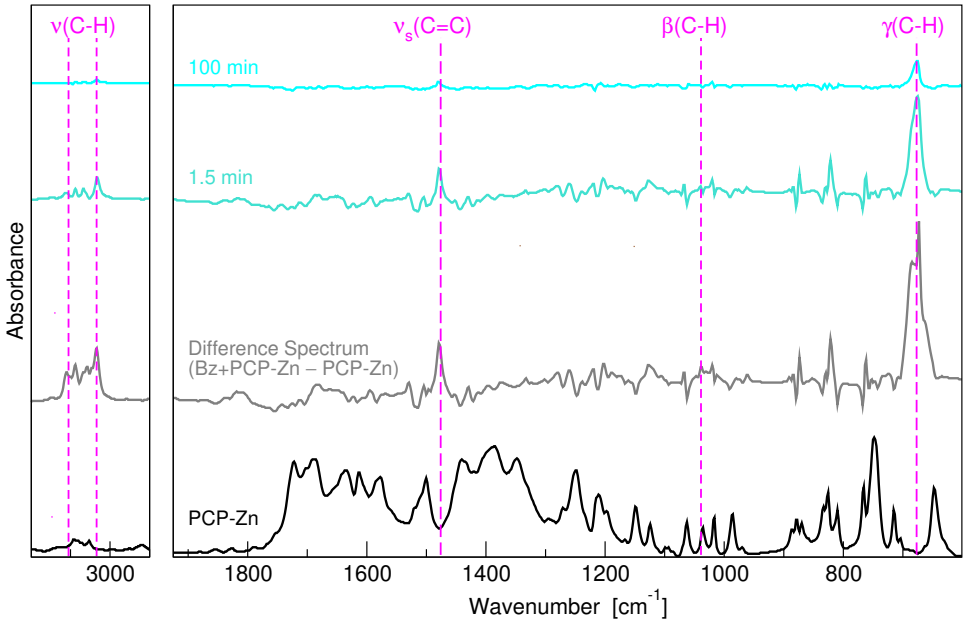

Figure S9. IR spectra of PCP-Zn (black), the difference spectrum of PCP-Zn minus Bz+PCP-Zn (grey), along with the difference spectra after 1.5 minutes of evacuation (turquoise) and 100 minutes of evacuation (cyan). The benzene peaks (magenta) are identified and present even after 100 minutes of evacuation, showing that the benzene is bound in PCP-Zn to form Bz+PCP-Zn. Modes are labeled as follows: ν refers to stretching, β is in-plane bending, and γ is out-of-plane bending.

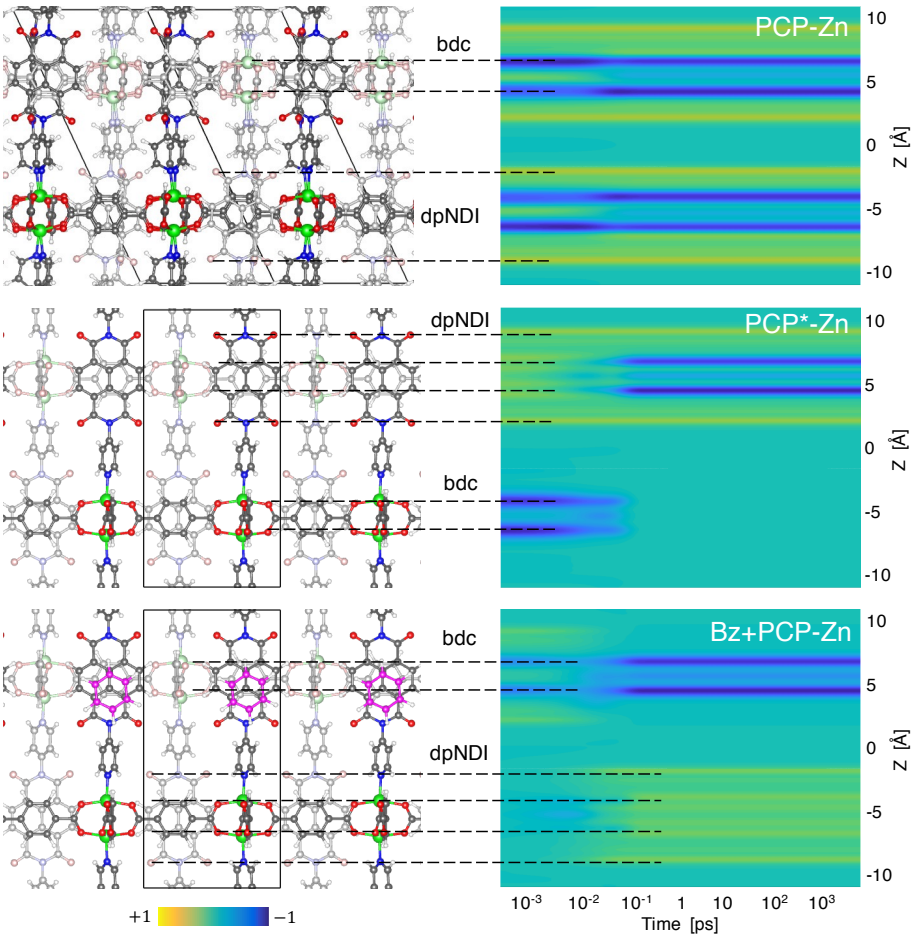

Figure S10. Real-space electron and hole relaxation after a 330 nm (3.76 eV) photoexcitation. Yellow indicates a gain of an electron, blue indicates a loss of an electron (i.e. hole), and green indicates no change in charge. The plots are obtained by integrating the charge density in the xy-plane and showing the result for all z values in the unit cell as a function of time.

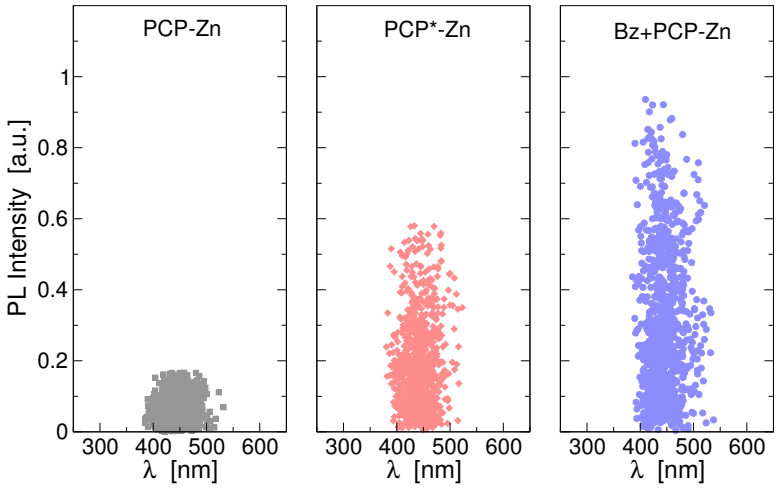

Figure S11. Oscillator strengths f_{ij} for PCP-Zn, PCP*-Zn, and Bz+PCP-Zn at each of the 1000 time steps along the MD trajectory. Values are normalized so that the resulting photoluminescence spectrum of Bz+PCP-Zn in Fig. 3 in the main manuscript has its maximum at 1.

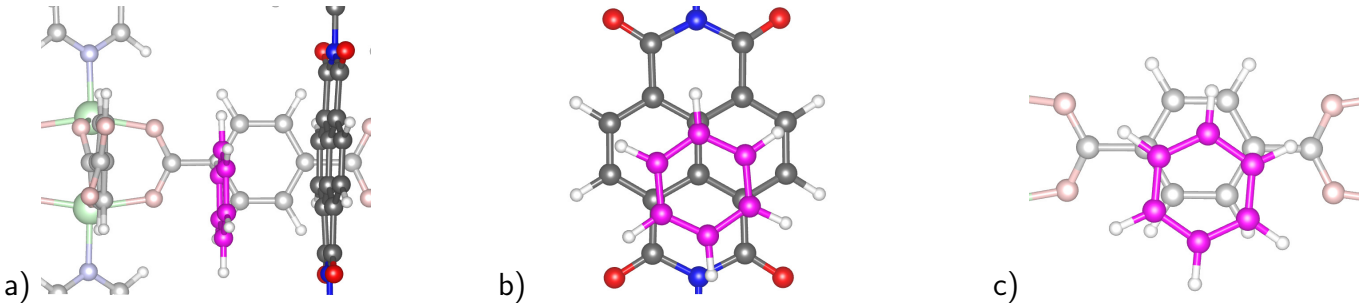

Figure S12. Enlarged images of Bz+PCP-Zn to highlight the $\pi - \pi$ interactions between the Bz and the PCP-Zn framework, shown with charge-density difference in Figure 5 of the main text. a) Bz between the two ligands, b) Bz with dpNDI, and c) Bz with bdc. A slight displacement is noted between the Bz and both ligands.

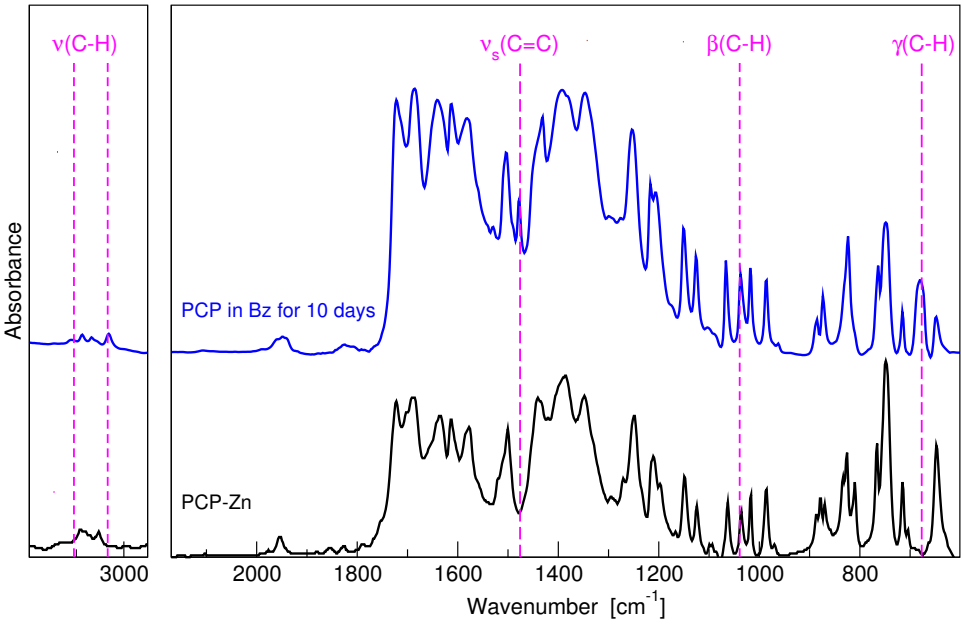

Figure S13. IR spectra of PCP samples in activated form (black) and after the PCP-Zn is immersed in Bz for 10 days (blue) according to the synthesis procedure.[6] As in Figure 6, the characteristic bands of adsorbed Bz are clearly observed. Modes are labeled as follows: ν refers to stretching, β is in-plane bending, and γ is out-of-plane bending.

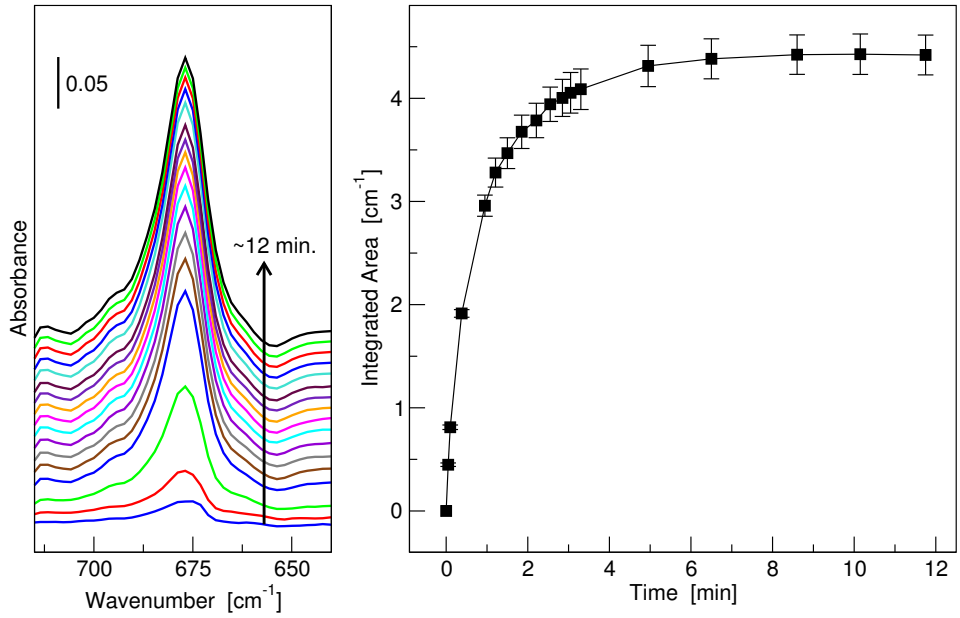

Figure S14. Evolution of the β(CH) band of adsorbed Bz as a function of time after introducing vapor exposure of 1 Torr of Bz (left) along with the integrated area of the β(CH) peak with time (right). Upon 1 Torr exposure, the adsorption of Bz in activated PCP-Zn reaches equilibrium within 12 minutes.

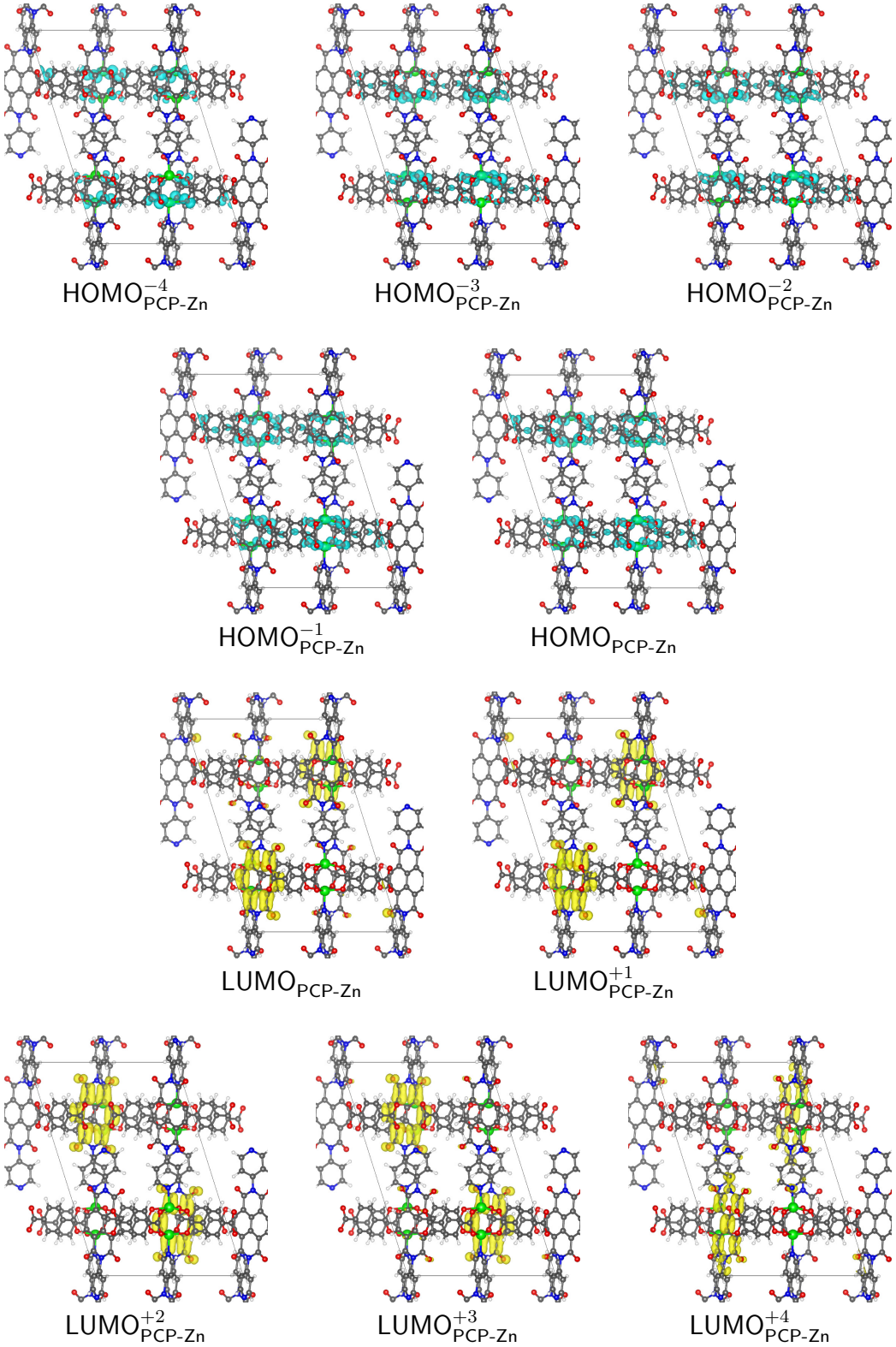

Figure S15. The $\text{HOMO}^{-4}_{\text{PCP-Zn}}$ to $\text{LUMO}^{+4}_{\text{PCP-Zn}}$ orbital partial charge densities at an isosurface value of 2×10^{-3} $e/\text{Å}^3$ for PCP-Zn. The valence band is composed mainly of bdc ligands while the conduction band is composed of dpNDI ligands.

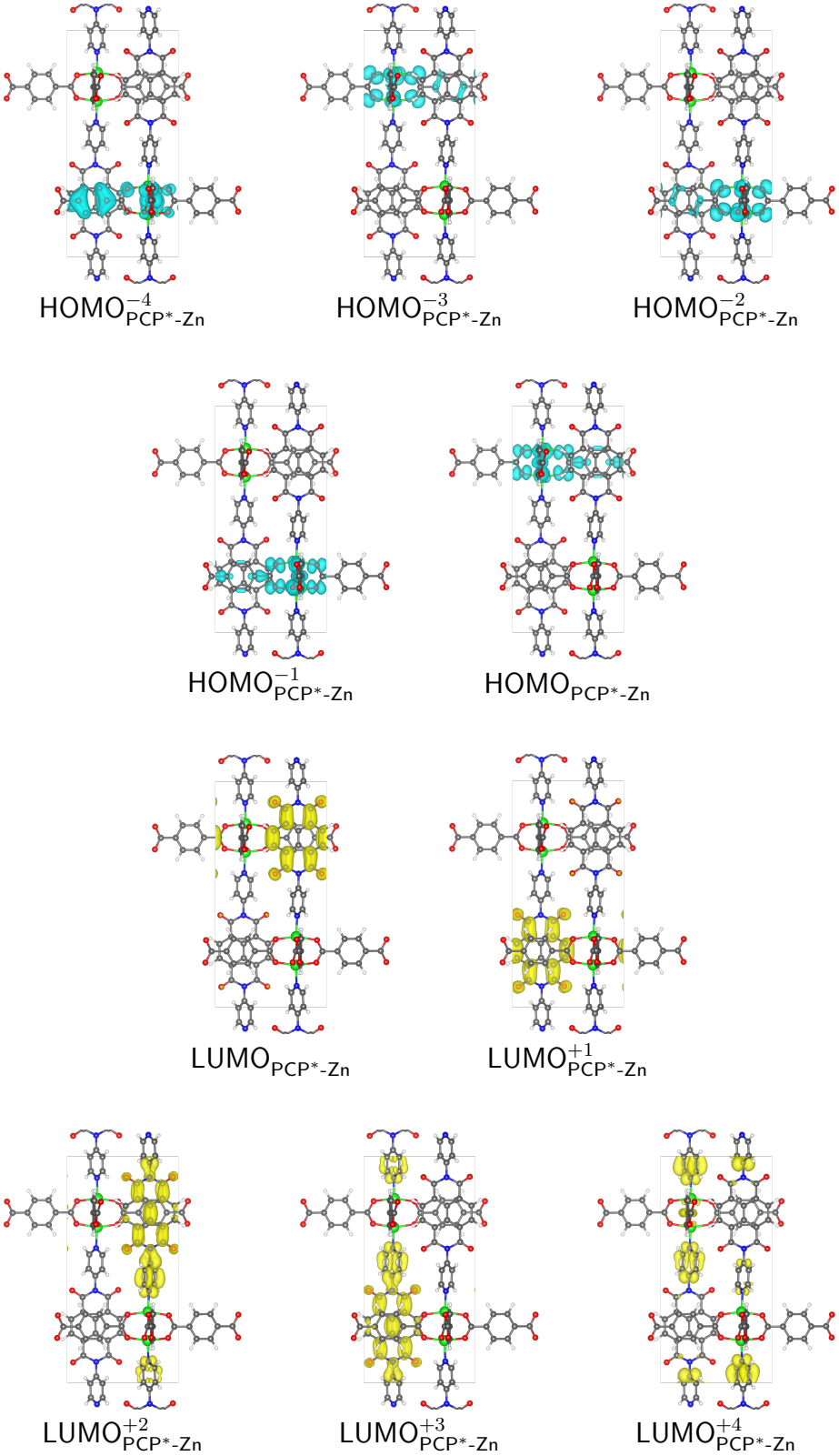

Figure S16. The HOMO$^{-4}_{\text{PCP*-Zn}}$ to LUMO$^{+4}_{\text{PCP*-Zn}}$ orbital partial charge densities at an isosurface value of 2×10^{-3} $e/\text{Å}^3$ for PCP*-Zn. The valence band is composed mainly of bdc ligands while the conduction band is composed of dpNDI ligands.

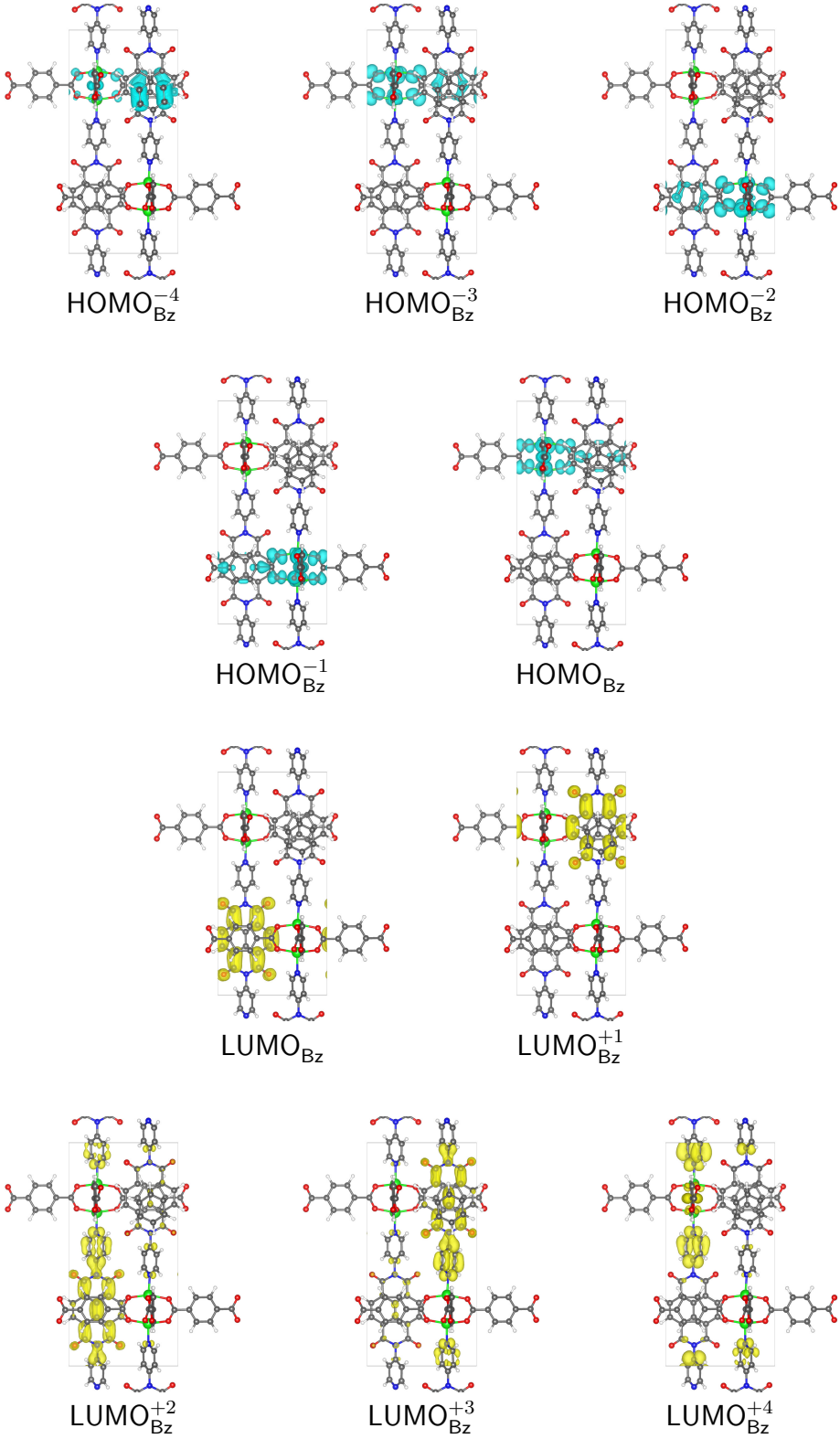

Figure S17. The HOMO$_{Bz}^{-4}$ to LUMO$_{Bz}^{+4}$ orbital partial charge densities at an isosurface value of 2×10^{-3} $e/\text{Å}^3$ for Bz+PCP-Zn. The valence band is composed mainly of bdc ligands while the conduction band is composed of dpNDI ligands (as with PCP-Zn in Fig. S15), but here benzene orbitals are present in the valence band in HOMO$_{Bz}^{-4}$.

* E-mail: thonhauser@wfu.edu

[1] Kasha, M. Characterization of electronic transitions in complex molecules. *Discuss. Faraday Soc.* **1950**, *9*, 14–19.

[2] Jensen, S.; Tan, K.; Lustig, W.; Kilin, D.; Li, J.; Chabal, Y.; Thonhauser, T. Quenching of photoluminescence in a Zn-MOF sensor by nitroaromatic molecules. *J. Mater. Chem. C* **2019**, *7*, 2625–2632.

[3] Chen, J.; Schmitz, A.; Inerbaev, T.; Meng, Q.; Kilina, S.; Tretiak, S.; Kilin, D. S. First-principles study of p-n-doped silicon quantum dots: Charge transfer, energy dissipation, and time-resolved emission. *J. Phys. Chem. Lett.* **2013**, *4*, 2906–2913.

[4] Vogel, D. J.; Kilin, D. S. First-principles treatment of photoluminescence in semiconductors. *J. Phys. Chem. C* **2015**, *119*, 27954–27964.

[5] Svane, K. L.; Walsh, A. Quantifying thermal disorder in metal-organic frameworks: Lattice dynamics and molecular dynamics simulations of hybrid formate perovskites. *J. Phys. Chem. C* **2017**, *121*, 421–429.

[6] Takashima, Y.; Martínez, V. M.; Furukawa, S.; Kondo, M.; Shimomura, S.; Uehara, H.; Nakahama, M.; Sugimoto, K.; Kitagawa, S. Molecular decoding using luminescence from an entangled porous framework. *Nat. Comm.* **2011**, *2*, 168.